Title: Single-cell and spatiotemporal profile of ovulation in the mouse ovary

Author List: Ruixu Huang[1,10], Caroline Elisabeth Kratka[2,10], Jeffrey Pea[2], Cai McCann[3], Jack Nelson[3], John P. Bryan[3,9], Luhan Tracy Zhou[2], Daniela D. Russo[4,5,6], Emily J. Zaniker[2], Achla H. Gandhi[1], Alex K. Shalek[4,5,6], Brian Cleary[7], Samouil L. Farhi[3,11,+], Francesca E. Duncan[2,11,*], Brittany A. Goods[1,8,11,12,*]

Affiliations:

[1] Thayer School of Engineering at Dartmouth College, Hanover, NH, USA.

[2] Department of Obstetrics and Gynecology, Feinberg School of Medicine, Northwestern University, Chicago, IL, USA.

[3] Spatial Technology Platform, Broad Institute of MIT and Harvard, Cambridge, MA, USA

[4] Klarman Cell Observatory, Broad Institute of MIT and Harvard, Cambridge, MA, USA

[5] Ragon Institute of MGH, MIT and Harvard, Cambridge, MA, USA

[6] Institute for Medical Engineering & Science, Department of Chemistry, and Koch Institute for Integrative Cancer Research, Massachusetts Institute of Technology, Cambridge, MA, USA

[7] Faculty of Computing and Data Sciences, Department of Biomedical Engineering, Department of Biology, Program in Bioinformatics, Boston University, Boston, MA, USA

[8]Molecular and Systems Biology, and Program in Quantitative Biomedical Sciences at Dartmouth College, Hanover, NH, USA.

[9]Department of Electrical Engineering and Computer Science, Massachusetts Institute of Technology

[10]Authors contributed equally

[11]Authors contributed equally

[12]Lead contact

[*]Correspondence: f-duncan@northwestern.edu and britt.anne.goods@dartmouth.edu

Summary: Ovulation is a spatiotemporally coordinated process that involves several tightly controlled events, including oocyte meiotic maturation, cumulus expansion, follicle wall rupture and repair, and ovarian stroma remodeling. To date, no studies have detailed the precise window of ovulation at single-cell resolution. Here, we performed parallel single-cell RNA-seq and spatial transcriptomics on paired mouse ovaries across an ovulation time course to map the spatiotemporal profile of ovarian cell types. We show that major ovarian cell types exhibit time-dependent transcriptional states enriched for distinct functions and have specific localization profiles within the ovary. We also identified gene markers for ovulation-dependent cell states and validated these using orthogonal methods. Finally, we performed cell-cell interaction analyses to identify ligand-receptor pairs that may drive ovulation, revealing previously unappreciated interactions. Taken together, our data provides a rich and comprehensive resource of murine ovulation that can be mined for discovery by the scientific community.

Keywords: ovary, ovulation, single-cell RNA-sequencing, spatial transcriptomics, cumulus cell

INTRODUCTION

Ovulation is a highly dynamic and cyclic process that occurs approximately 650 and 400 times throughout the reproductive lifespan in mice and humans, respectively[1]. During ovulation, there is substantial structural remodeling of the ovary, where the antral follicle, comprised of an oocyte and surrounding supporting somatic cells, will release a mature egg for fertilization. A surge of luteinizing hormone (LH) initiates ovulation and orchestrates key events in the ovulatory cascade, including the resumption of meiosis in the oocyte, expansion of the cumulus layer of the cumulus-oocyte-complex (COC), follicular rupture, COC release, and luteinization of the residual follicular cells[2]. The intricate spatiotemporal and molecular changes in gene expression that accompany the extraordinary structural changes in the ovary during ovulation, which occur over a narrow window of hours, remain to be fully elucidated. Understanding the molecular drivers of ovulation has critical implications for the diagnosis and treatment of infertility, the discovery of novel contraceptives, elucidating species differences in reproduction, unraveling novel cell types that promote healthy ovulation, and uncovering possible mechanisms of ovarian aging[3,4,5].

Single-cell transcriptomic approaches have significantly advanced our ability to unravel the complexities of cell populations within tissues. Single-cell RNA sequencing (scRNA-seq) allows for the identification of molecular signatures defining specific cell states, the inference of communication patterns between cells, and the identification of genes and pathways that drive specific biological processes[6-11]. Single-cell imaging spatial transcriptomics (iST), meanwhile, is particularly well-suited for defining the spatial organization of gene expression within tissues at single-cell resolution, providing valuable insights into the spatial relationships between cells within the tissue microenvironments and limiting artifacts that can be introduced during dissociation[12]. As such, the combination of scRNA-seq and iST has been adopted to study tissue dysfunction, diseases, and treatment responses, and when combined with novel computational methods, can uncover deep insights into complex cellular biology[13,14]. In the context of the ovary, single-cell studies have been instrumental in demarcating genes that define certain cell types, elucidating signals that drive follicle activation, and discovering underlying mechanisms of diseases such as ovarian cancer[15-22]. These efforts have provided foundational insights into the ovary but have two main limitations. First, they have focused on the longer time-scale changes that occur across the whole estrous cycle, or second, they have relied on inferred single-cell genomic data rather than direct single-cell profiling[20,23]. Thus, there is a critical need to build a resource that comprehensively defines ovulation specifically and spatiotemporally at true single-cell resolution.

To address this, we conducted scRNA-seq and iST in parallel on paired mouse ovaries across three well-defined ovulatory timepoints. We then integrated these two modalities to generate a robust dataset comprised of 391,584 cells via iST and 26,411 cells via scRNA-seq, capturing dynamic variations in gene expression and corresponding morphological changes throughout the ovulatory process in mice. Our analysis reveals major cell types (cumulus, stromal, granulosa, theca, luteal) with associated time-dependent gene signatures and localization within the ovary across ovulation. We also identify previously unappreciated genes and pathways within these ovulation-dependent cell clusters, such as neuronal pathways in cumulus cells and metal homeostasis in theca cells. Finally, we conducted cell-cell interaction (CCI) analyses to discover ligand-receptor pairs that may drive cell state changes in cumulus cells and underpin the luteinization process in granulosa and theca cells. Taken together, our resource provides a comprehensive view of ovulation, supporting several critical avenues of research related to reproductive health.

RESULTS

A single-cell temporal reference of cell types in the adult mouse ovary across ovulation reveals "early" and "late" cell states

To deeply profile the mouse ovary across ovulation using scRNA-seq and iST, we induced ovulation with human chorionic gonadotropin (hCG) in a synchronized fashion following hyperstimulation, and ovaries were collected at 0hr, 4hr, or 12hr after induction (**Figure 1A**). The 4hr timepoint is early in the ovulation process and represents the peak of the LH surge when the expression of key ovulation regulators is highest; the 12hr timepoint, meanwhile, represents a later stage when follicular rupture is underway[24]. We confirmed this with histological analysis of ovaries collected from a parallel set of mice **(Figure S1**). At 0hr post-hCG, there were follicles at different stages of development present including numerous antral follicles which were recruited to grow following hyperstimulation. Corpora lutea from previous estrous cycles were also present (**Figure S1A**). By 4hr post-hCG, the response to the ovulatory cue was apparent given the increase in the size of the antral follicles due to the accumulation of follicular fluid and expansion of the antral cavity and the cumulus layer surrounding the COCs (**Figure S1B**). By 12hr post-hCG, there were few antral follicles left in the ovary suggesting that ovulation had taken place, and consistent with this, the corpora lutea were prominent at this timepoint (**Figure S1C**). The few follicles that remained in the ovary at this time were close to rupture given their large size, thinning of the mural granulosa layer close to the ovarian surface, and the presence of fully expanded COCs containing mature metaphase II arrested eggs (**Figure S1C**). We collected one ovary per mouse for scRNA-seq and the contralateral ovary for iST at each of these specific timepoints (**Figure 1A and Figure S2**).

For the generation of scRNA-seq data, we followed standard 10X genomics workflows post-dissociation of ovarian tissues (see Methods). This resulted in a high-quality data set comprised of 26,411 cells (**Figure S3A-C**). We then used standard computational workflow to identify major top-level ovarian cell identities across ovulation and their associated marker genes[25] (see **Methods**). We identified eight major cell types in the ovary: cumulus cells, endothelial cells, epithelial cells, granulosa cells, luteal cells, myeloid cells, stromal cells, and theca cells (**Figure 1B**). Additionally, a cluster of oocytes (n = 16 cells) was identified but not further analyzed because of the small cluster size. The major cell types were characterized by highly enriched marker gene expression (**Figure 1C and File S1).** When compared to an existing scRNA-seq reference of the ovary generated throughout the estrous cycle, we successfully recapitulated all major ovarian cell types[18] (**Figure S3E**). Furthermore, within each major cell type, we identified unique cell subclusters for cumulus (Cumulus 1 and 2), endothelial (Endothelial 1 and 2), granulosa (Granulosa 1, 2, and 3), luteal (Luteal 1 and 2), stroma (Stroma 1 and 2), and theca (Theca 1 and 2) cells (**Figure 1B**). Several known marker genes were enriched in these particular clusters, including *Sult1e1* (cumulus)*, Inhbb* and *Amh* (granulosa), *Lhcgr* (luteal), *Dcn* (stroma), and *Cyp17a1* (theca). We also identified previously undescribed highly expressed genes specifically found in certain clusters, including *Zpf804a* (cumulus), *Oca2* (theca), *Pdzrn3 (stroma), and Gm2a (*luteal) (**Figure 1C and File S1**). Notably, we found two cumulus cell clusters that were unique to ovulation given their temporal emergence, which were identified based on cumulus cell expansion markers and gene ontology (GO) pathway analysis results. These clusters of expanding cumulus cells are not present in a reference scRNA-seq dataset of the adult mouse ovary captured throughout the estrous cycle but are not limited to proestrus when ovulation takes place. The presence of these clusters only in our dataset demonstrates their unique relevance to ovulation **(Figure S3E**). By focusing our temporal data collection on the short window of ovulation, our dataset has a high enough resolution to detect cumulus cell populations that are undergoing unique processes and would otherwise not be present[18].

In addition to differences in gene expression, some cell clusters separated into "early" and "late" groups relative to the ovulation time course, while other clusters were present throughout all ovulation (**Figure 1D)**. Specifically, "early" clusters included Theca 1, Granulosa 1, Stroma 1, and Luteal 1, which were expressed

almost exclusively at 0hr and/or 4hr. “Late” clusters were expressed predominantly at 12hr and included Cumulus 2, Luteal 2, Stroma 2, and Theca 2. Clusters expressed throughout ovulation included Granulosa 2, Granulosa 3, Endothelial 1, Endothelial 2, Epithelial, and Myeloid. To determine if there were underlying functional differences across clusters, we performed pathway analysis on the marker gene list for each identified cluster of cells and categorized the pathways by high-level functional classifications (see **Methods**, **File S2**). We then compared the representation of these high-level functions across early or late clusters (**Figure 1E**). Pathways related to "signal transduction”, “hormone production,” “ECM formation”, and “lipid metabolism” had similar representation in the early and late clusters. However, there were several distinct pathway categories in early and late clusters. This included “ovulation” (*Inha*, *Inhba*, *Inhbb*, *Foxl2*) in the early clusters, and pathways related to “cell migration” *(Col3a1*, *Timp1*, *Fgf2*), “cell homeostasis” (*Col1a1*, *Col1a2, Sparc*), “metal homeostasis” (*Mt1*, *Mt2*, *Mt3*) and “immune function” (*Hspa8, Cd63, Anxa2, Gstp1*) in the later clusters (**File S2**). Taken together, these results demonstrate that early and late cell clusters can be broadly distinguished by shifts in their functional pathways, where there is a greater diversity of pathway terms in the clusters associated with the later time point in ovulation.

Single-cell spatial transcriptomic analysis of adult mouse ovaries throughout ovulation reveals temporally-driven processes

To identify genes and signaling interactions driving spatiotemporal changes across ovulation, we also generated single-molecule resolution iST data on collected contralateral ovaries (**Figure 1A and Figure S2C-D**). We designed a 198-plex MERSCOPE panel based on known marker genes for ovarian cell types and genes of interest relevant to ovulation from previously published datasets[18,19,24]. We assembled contralateral ovaries into an optimal cutting temperature (OCT) tissue microarray to allow parallel processing of all ovaries on a single coverslip and thus minimize batch effects **(Figure S2C**)**.** We acquired data from 8 samples (3 ovaries at 0hr, 3 ovaries at 4hr, and 2 ovaries at 12hr). As expected, the anatomical features of the MERSCOPE sections at 0hr and 4hr post-hCG were very similar to those observed via histology (**Figure 1F, Figure S1A-B, and Figure S4B**). At 12hr post-hCG, one MERSCOPE section was from an ovary containing mostly corpora lutea and few unruptured follicles **(Figure S4B)** similar to what we observed via histology **(Figure S1C)**, whereas the other MERSCOPE section was from an ovary with many peri-ovulatory follicles close to rupture **(Figure 1F)**. The presence of these two phenotypes at 12hr post-hCG is consistent with inherent biological variation in the timing of ovulation.

Following filtering based on transcript count and cell area, we retained 391,584 cells across all samples, with an average of 88 transcripts per cell (**Figure S3C-D**). We then normalized and scaled counts, performed dimensionality reduction and Leiden clustered, and annotated cell types in each ovary based on genes enriched in each cluster. We additionally used ovarian morphology to annotate the major top-level cell types, including theca cells, stromal cells, granulosa cells, luteal cells, immune cells, endothelial cells, and epithelial cells (**Figure 1F and Figure S4A-C)**. To further investigate spatiotemporal gene expression changes during ovulation, we integrated our single-cell and spatial transcriptomes together with a machine learning approach[26]. Our integrated data resource powers us to precisely identify high-resolution spatiotemporal changes in genes beyond those initially targeted by our MERSCOPE probes. As a result, we could infer the localization patterns of over 25,000 genes from ovaries at 0hrs, 4hrs, and 12hrs post-hCG. We evaluated the integration with multiple approaches (see **Methods**). First, more than 70% of genes having a training score above 0.7 demonstrates the successful integration at the model level (**Figure S5A**). Second, we randomly selected test genes and excluded them from the model training process. When comparing the predicted expression profile versus the actual expression profile from the spatial transcriptome, we observe similar

localization patterns for those test genes such as *Col1a2*, which is highly enriched in mesenchymal cells (**Figure S5B**). Lastly, we compared predicted gene expression profiles with actual RNA expression detected using RNAscope on histological ovarian sections as validation, where the predicted expression profile of *Sik3* was primarily present in luteal cells at 0hr and *Slc6a6* being primary present in cumulus and mural granulosa cells at 12hr was recapitulated in RNAscope images (**Figure S5C**).

Through scRNA-seq and iST analyses, we have captured all major ovarian cell types and their spatial distributions across ovulation which are consistent with established timelines of murine ovulation and expected changes in follicular morphology. To date, this is the most comprehensive single-cell dataset describing the events of ovulation in the mouse and serves as a robust resource for discovering cell states that are unique to ovulation.

Analysis of time-dependent cell types reveals unique expression patterns and putative functions of early and late cell clusters

To further investigate the time-dependent changes in gene expression for each cell type, we performed pathway analyses on cluster-defining marker genes and differential gene expression analysis (DEA) between early and late cell subclusters for time-varying cell types.

Stromal cells

We observed time-dependent changes in gene expression throughout ovulation and identified two stromal cell subclusters: early stromal (Stroma 1) and late stromal (Stroma 2) cells (**Figure 2A-B**). DEA performed between the early and late stromal subclusters indicated that the top-upregulated genes in early stromal cells are *Lama2*, *Grm7*, *Ptprd*, *Tcf21*, and *Tenm4*, whereas the top-upregulated genes in late stromal cells are *Timp1*, *Ereg*, *Il11*, *Pde10a*, and *Mrap* (**Figure 2B** and **File S4**). Within each subcluster, we further characterized the expression profiles of known ovarian stromal cell markers. *Dcn,* or decorin*,* is a proteoglycan associated with extracellular matrices in a variety of tissues and was highly enriched in early stromal cells[27] (**Figure 2C**). In addition, *Pdgfra*, a platelet-derived growth factor, and ovarian mesoderm marker, exhibited increased expression in late stromal cells[28,29] (**Figure 2D**). We also identified genes that were highly enriched but not well characterized in the ovarian stroma, such as *Egflam* (early stromal) and *Pzdrn3 (*late stromal*). Egflam*, also known as pikachurin, is an extracellular matrix-like protein that interacts with dystroglycan and has been implicated in photoreceptor synapse function[30,31] (**Figure 2E**). *Pdzrn3* encodes an E3 ubiquitin ligase previously shown to be involved in cell migration and vascular morphogenesis [32,33] (**Figure 2F)**.

GO Analysis of top differentially expressed genes between the early stromal (Stroma 1) and late stromal (Stroma 2) subclusters revealed that early stromal cells were enriched in pathways related to ECM formation (*Fbn2*, *Lama2*, *Lum*), smooth muscle relaxation (*Gucy1a1*, *Prkg1*, *Mrvi1*), and the estrous cycle (*Mdk*, *Ptn*, *Anxa1*). Late stroma cells were unique in pathways related to angiogenesis (*Xbp1*, *Pkm*, *Bmper*), cell differentiation (*Runx1*, *Ugdh*, *Hspa9*), hormone production (*Wnt4*, *Hif1a*, *Por*), and protein modification (*Hsp90aa1*, *Hspa9, Hspd1*) (**Figure 2G and File S5**). The upregulation of ECM-related pathways in early stroma cells suggests that this population has greater involvement in general ECM organization and remodeling than late stroma cells. The enrichment of hormone production pathways in late stromal cells suggest functions of late stromal cells in steroid hormone production. In addition, late stroma cells potentially increase blood vessel formation to accommodate the transport of these hormones to the rest of the body.

Theca cells

Theca cells were further differentiated into four subclusters, each detected at one specific time point (0hr, 4hr, or 12hr); two subclusters were predominantly observed at 0hr whereas the remaining two subclusters

were found at 4hr or 12hr (**Figures 3A-B and File S3**). The top differentially expressed genes in the theca subclusters are shown in **Figure 3B**. Genes known to be active in theca cells include *Cyp17a1* and *Col4a1*, which are expressed in early and late theca cells, respectively. More specifically, *Cyp17a1* expression was distinguished at 0hr from the 4hr and 12hr theca subclusters, which were marked by *Col4a1* expression (**Figures 3C and 3D**). *Cyp17a1* is a cytochrome P450 enzyme that catalyzes critical steps in androgen synthesis[34-36], whereas *Col4a1* is an ECM component that is part of the theca basement membrane[37,38]. In addition, we identified several genes that were upregulated in theca subclusters that have yet to be described in this cell type, including *Oca2* (at 0hr) and *Fam161a* (at 12hr) (**Figures 3E and 3F**)**.** *Oca2* encodes P protein, which is integrated into the cell membrane and functions by maintaining pH and transporting small molecules[39]. In contrast, *Fam161a* encodes for a centrosomal protein primarily known for ciliary function and microtubules[40-42].

We then conducted GO analysis of top differentially expressed genes between each theca subcluster (**Figure 3G**). This analysis revealed that in the first 0hr cluster (Theca_00_1), pathways upregulated in theca cells included hormone production, immune function, and metabolism of lipids/phosphorus, which are consistent with the functions of a steroidogenic theca cell population. In the second 0hr subcluster (Theca_00_2), theca cells presented enrichment in processes related to hormone production, ovulation, and signal transduction. Theca cells at 4hr showed upregulated pathways including chemotaxis and signal transduction whereas pathways upregulated in the 12hr subcluster were related to cell proliferation, immune processes, metal homeostasis, and plasma membrane function (**Figure 3G**). Theca cells at 12hrs upregulate metal homeostasis pathways, driven by the genes *Mt1*, *Mt2* and *Mt3*, which suggests that metal homeostasis could be important for theca cells to perform their primary functions at later time points in ovulation, including hormone synthesis. Taken together, the results of our GO analysis show that theca cell subclusters are enriched for known functions, like hormone production, as well as unexplored pathways performed by theca cells temporally.

Luteal cells

Using published luteal cell subtype markers, we identified four luteal subclusters: Recent Luteal cells, Mural cells, Mixed Luteal cells, and Other Luteal cells (**Figure 4A-B, File S3)**. Recent Luteal cells were defined by high expression of proliferation markers and steroidogenic enzymes and represent corpora lutea that are currently producing and secreting progesterone[18]. Mural cells were comprised of granulosa and theca cells of large antral follicles that are differentiating into luteal cells and were marked by expression of genes including *Adamts1*[43,44], *Mt2*[45-47], *Mrap*[48], *Parm1*[49], *S100a6*[50], and *Cdkn1a*[18]. Other Luteal cells were characterized by expression of the proliferation marker *Top2a*, as well as other marker genes including *Ube2c*[51], *Birc5*[18], *Inhbb*[52], and *Nap1l5*[53]. Mixed Luteal cells expressed various luteal markers and could not be distinguished into a specific luteal cell subtype, but likely consist of a mix of active and regressing corpora lutea with varying levels of progesterone secretion. The top differentially expressed genes in all subclusters are shown in **Figure 4B**. The luteal subclusters exhibited temporal differences with Mixed Luteal cells predominately present at the 0hr and 4hr timepoints, Other Luteal cells expressed at 0hr and 12hr, and Recent Luteal and Mural Luteal cells primarily found at 12hr (**Figure 4B**).

We further investigated the differential gene expression profiles between all subclusters. As expected, we observed upregulation of *Lhcgr* in Mixed Luteal and Other Luteal cells (**Figure 4C)**. LH binds to LHCGR to promote androgen synthesis. In addition, *Runx1*, a DNA-binding protein known to be an essential transcriptional regulator of ovulation and luteinization, is upregulated at 12hr in the Recent Luteal and Mural Luteal subclusters[54-56] (**Figure 4D**). We also identified previously unappreciated genes with temporal expression patterns in luteal cells. *Gm2a*, a glycolipid transporter that promotes the degradation of ganglioside GM2 to GM3 enriched in the Mixed Luteal and Other Luteal subclusters[57] (**Figure 4E**). Notably, GM3 is upregulated in the rat ovary during ovulation, but its role is largely unknown[58,59]. In addition, *Fndc3b* was

enriched in the Recent Luteal and Mural Luteal subclusters and belongs to the fibronectin type III domain containing a family of myokines and adipokines with general roles in migration, adhesion, and proliferation of cells (**Figure 4F**). FNDC3B has roles in bone and tumor development, but no documented functions in the ovary[60-62]. However, another member of this myokine/adipokine family, FNDC5 or irisin, regulates the steroid hormone production and secretion in various granulosa cell models[63-65], suggesting that *Fndc3b* may function in the production of progesterone within the corpus luteum.

We next performed GO analysis on the top level Luteal 1 and 2 clusters using the marker genes for each cluster (**File S2**). Early luteal (Luteal 1) cells are highly enriched in pathways related to hormone production, consistent with the role of luteal cells in synthesizing progesterone. Late luteal (Luteal 2) cells exhibit a range of upregulated pathways, including those involved in extracellular matrix organization and signal transduction. We also observed “response to estrogen” and “cell volume homeostasis” as two additional pathways of interest in the Luteal 2 cluster (**File S2**). High levels of estrogen trigger ovulation, which is followed by luteinization of granulosa and theca cells. In addition, luteinization is marked by hypertrophy of luteal cells – a modulation of cell volume. In interpreting these results, it is important to note that the Luteal 1 cluster (which contains cells from all three time points but mostly 0hr and 4hr) likely contains existing corpora lutea from previous cycles. In mice, corpora lutea persist for multiple cycles, receive repeated luteolytic signals, and may continue to produce progesterone[66,67]. On the contrary, the Luteal 2 cluster is exclusively present at 12hr and likely represents actively forming or newly formed corpora lutea, supporting the presence of pathways related to the organization of luteinizing granulosa and theca cells into a functional corpus luteum.

Lastly, we conducted GO analysis on all luteal subclusters using the differentially expressed genes between each subcluster (**Figure 4G**). In Mixed Luteal cells, we observed several pathways related to lipid metabolism and redox homeostasis. In addition, genes that encode subunits of complex I of the electron transport chain (ETC), NADH:ubiquinone oxidoreductase (e.g., *Ndufa6, Ndufb4, Ndufab1, Ndufs3, Ndufc2, and Ndufc1*) drove upregulation of ETC-related pathways. Recent Luteal cells were enriched in pathways related to extracellular matrix formation, immune function, muscle contraction, and signal transduction. Other Luteal cells showed upregulation of pathways related to translation and localization of proteins. Mural Luteal cells were enriched in pathways including the metabolism of prostaglandins and lipids, and the formation of blood vessels and ECM (**Figure 4G**). Thus, these results suggest that Mixed Luteal cells exhibit a primary function of steroid hormone production, consistent with the synthesis of progesterone within mature corpus lutea from previous cycles. In contrast, Recent Luteal and Mural Luteal cells may represent newly forming corpus lutea that are undergoing extensive ECM remodeling and vascularization. Other Luteal cells appear to have active roles in protein synthesis.

Cumulus cells

For cumulus cells, we identified two time-dependent subclusters: early cumulus (Cumulus 1) and late cumulus (Cumulus 2) (**Figure 5A-B**). Both subclusters were distinct temporally, with early and cumulus cells primarily detected at 4hr and 12hr, respectively (**Figure 5C**). The top differentially expressed genes between the early and late cumulus cell subclusters were *Sult1e1*, *Robo2*, *Pgr*, *Rnf180*, and *Tac1* (upregulated in early cumulus cells), and *Spp1*, *S100a6*, *Cck*, *Timp1*, and *Chchd10* (upregulated in late cumulus cells; **Figure 5B and File S4**). Given that the cumulus subclusters were not previously identified in the reference scRNA-seq dataset[18] (**Figure S3E**), we validated the single-cell expression pattern using *in situ* RNA hybridization on histological sections **(Figure 5C-F).** In addition to the 0h, 4h, and 12hr timepoints we also included an 11h timepoint to allow greater resolution of the late periovulatory period. As expected, *Sult1e1*, a gene known to be expressed in cumulus cells that are involved in estrogen metabolism, was high at 4hr[68-70] **(Figure 5C)**. Also as expected, *Lox,* a gene involved in ECM formation and expressed in developing follicles and COCs, was high at

12hr[71-74] **(Figure 5D)**. In addition, our transcriptomic analysis identified two genes, *Zfp804a* and *Emb*, which also showed similar temporal expression patterns to *Sult1e1* and *Lox*, respectively. We observed similar expression patterns with RNAscope validation (**Figure 5E and 5F**).

Gene ontology analysis of top marker genes in the Cumulus 1 and 2 clusters revealed "ovarian cumulus expansion" as a top biological process in both clusters, further validating our cell type identification (**File S2**)**.** Early cumulus cells also showed upregulation of "glycosaminoglycan metabolism," "fused antrum stage," and "EGFR interacts with phospholipase C-gamma" processes. These pathways are consistent with known biological processes occurring in the COC during ovulation, when EGF stimulates production of glycosaminoglycans (e.g., hyaluronan) in cumulus cells to promote COC expansion and fluid accumulation within the antral follicle[75-78]. In addition, hyaluronan is secreted by granulosa cells into the follicular fluid, where it contributes to an osmotic gradient that draws fluid from theca cells into the antral space[79,80]. Early cumulus cells also exhibited several pathways related to the nervous system, including "axon guidance" and "nervous system development". Genes that drove the "axon guidance" and "nervous system development" pathways included *Epha5*, *Robo2*, *Epha4*, *Epha7*, *Alcam*, *Sema3c*, and *Efna5* (**File S2**). Upregulation of genes important to nervous system function has previously been documented in COCs[74,81], but their role in cumulus cells remains unclear. Late cumulus cells (Cumulus 2) showed enrichment of genes for "positive regulation of prostaglandin biosynthetic process," which is consistent with the role of prostaglandins in stimulating COC expansion[82-85] and promoting dissolution of the COC ECM to facilitate fertilization of the oocyte by sperm[86]. The Cumulus 2 cluster also exhibited several pathways related to cholesterol production and immune function (**File S2**).

To determine the pathways that distinguish early cumulus cells from late cumulus cells, we conducted a second GO analysis using the top differentially expressed genes between these two cell populations (**File S5**). The transcriptome of early cumulus cells (Cumulus 1) exhibited enrichment of genes related to the nervous system, chemotaxis, immune function, and signal transduction, with the latter representing key pathways driving COC expansion including LH and receptor tyrosine kinase signaling. Late cumulus cells (Cumulus 2) exhibited enrichment in genes related to fatty acid metabolism and cholesterol/hormone synthesis (**Figure 5E**). Steroid hormone synthesis by cumulus cells has been documented in several species, including mice and humans, and is thought to be important for oocyte maturation and quality[87-95]. Therefore, the upregulation of steroidogenic pathways in late cumulus cells may be supporting several processes that occur near the completion of ovulation, including hormone production in mural cells and fertilization by sperm.

Cell-cell interaction (CCI) analysis reveals significant interactions that change over the time course of ovulation

To characterize the signaling pathways that are active across ovulation, we conducted cell-cell interaction (CCI) analysis for each cell type at each timepoint, first using our scRNA-seq dataset (**Figure 6A**). We observed that the total number of interactions increased over time (**Figure S6A**). We also found a pattern of distinct cell subclusters that sent and received signals across the ovulation time course (**Figure 6A**) and that the strength of outgoing and incoming signals was variable for many subclusters (**Figure 6B**). At 0hr, we found that the primary senders were Stroma 1, Epithelial, Granulosa 1, and Granulosa 2, where the interaction strength of outgoing signals was high for Stroma 1 and incoming was strong for Endothelial cells. Notably, the cell subcluster that mainly received signals at 0hr was the Luteal cluster. For the 4hr timepoint, the primary senders were Stroma 1, Stroma 2, Cumulus 1, Epithelial, and Theca 1 whereas Mixed luteal, Endothelial 1, and Epithelial were primarily receivers. At the 12hr timepoint, the major senders were Cumulus 2, Stroma 1, Stroma 2, and Recent Luteal subclusters (**Figure 6A and 6B**). These patterns suggest that stromal and

cumulus cells remain active communicators, both sending and receiving signals throughout ovulation, in contrast to luteal cells which primarily receive signals from other cell types. Overall, we also observed that stromal cells maintained a similar interaction strength, both incoming and outgoing, over the full time course of ovulation. We found that across time, outgoing signal strength was dominated by collagen-driven interactions, whereas incoming interaction strengths were mostly mediated by laminin, SPP1, and THBS (**Figure S6B-D**). Notably, we found the three cell subclusters with the highest incoming signal strength at 12hr as Cumulus 2, Recent Luteal, and Mural Luteal **(Figure 6B and Figure S6).** Together, this suggests a highly dynamic ecosystem of cells actively sending and receiving signals across this narrow window of ovulation, and our analysis has identified several of the strongest drivers of these global alterations.

We next wanted to determine if there are specific ligand and receptor pairs that can explain patterns of communication that are unique to our dataset within the ovulatory window. Specifically, we investigated interactions between cumulus, granulosa, theca, stromal, and luteal cells (**Figure 6C-F**). These cell types were selected based on the relevance of their interaction to ovulation. For example, communication between granulosa and cumulus cells is critical for processes including granulosa cell differentiation and proliferation, cumulus cell layer expansion, oocyte growth and meiotic progression, and follicle rupture[96-100]. Furthermore, the communication of theca and granulosa cells to luteal cells is essential for the development of new corpora lutea as well as the degradation of existing ones as part of luteolysis. Notably, the stromal clusters observed the highest outgoing strength across all timepoints (**Figure 6B**) and thus may contribute to the luteinization process, possibly via laminin, collagen, FN1, and several other proteins that show strong outgoing strength (**Figure S6B-D**).

At 0hr post-hCG, we observed an enriched interaction between laminins (ligand), such as *Lama1*, *Lama2*, *Lama4*, and *Lamc4* from granulosa, theca, and stroma cells, and the integrin *Itga9* (receptor) from luteal cells (**Figure 6D-F)**. Laminins are known to localize to theca cells to form the basement membrane across all follicle stages[101,102] with additional expression in granulosa and stroma cells[46]. Integrin subunits, such as *Itga9* and *Itb1*, are known to be expressed in the luteal cells, with their interactions with laminins modulating progesterone synthesis during luteinization[103]. Although integrin α9 and its interaction with laminin is largely uncharacterized in the ovary, they are highly localized together (**Figure 6G**) and suggest that they may play a similar role.

At 4hr post-hCG, interactions between BMP2 and its receptors (BMPR1a, BMPR2, AVCR2A) were highly upregulated between granulosa and cumulus cells, respectively (**Figure 6C**). BMP2 has been previously shown to be highly expressed in mural granulosa cells in antral follicles[104], whereas loss of BMP receptors has been shown to lead to reduced cumulus cell expansion and spontaneous ovulation[105,106]. At this time point, we also observed communication between theca/granulosa cells and luteal cells via BMP2 and ACVR2A (**Figure 6E- F**). Expression of *Bmp2* and its receptors is known to be suppressed following hCG administration and is re-expressed during luteolysis of corpus lutea, suggesting a role as an inhibitor of luteinization and formation of the early corpus luteum[107]. Additionally, we observed an enriched interaction between *Fgf2* (ligand) and *Sdc3* (receptor) from stroma/granulosa cells and luteal cells, respectively (**Figure 6D, 6F**), with their co-localization observed spatially (**Figure 6H**). FGF2 acts as a mitogenic factor in promoting luteal cell proliferation and extracellular matrix remodeling during luteal angioregression[108]. *Sdc3,* which encodes for the proteoglycan syndecan-3, is expressed in the corpus lutea and is suggested to be involved in inflammation[109].

At 12hr post-hCG, we notably observed enriched signaling of FGF2 from stromal cells to various proteoglycans in luteal cells (**Figure 6D**), including syndecans and glypican 4. FGF2 is also involved in pro-angiogenic actions in the developing corpus lutea and is highly expressed during the follicular-luteal transition[110,111]. Syndecan-1 and 4 are known to be involved in cytoskeletal reorganization and focal adhesions, respectively, and thus may promote tissue remodeling to generate new corpus lutea[112,113]. Indeed,

Sdc1, Sdc4, and *Gpc4* have been shown to be enriched in luteinized mural granulosa cells with *Sdc4* being co-localized with *Fgf2* spatially[114] (**Figure 6I**). In addition, interactions between *Timp1* (ligand) from theca cells and *Mmp2* (receptor) from luteal cells were highly upregulated at 12hr post-hCG (**Figure 6E**). Tissue inhibitor metalloproteinases (TIMPs) and matrix metalloproteinases (MMPs) are well-established to interact and be involved with ovarian remodeling during ovulation, luteinization, and luteolysis[115-118].

DISCUSSION

Ovulation is a highly coordinated spatiotemporal event that is fundamental to fertilization, reproduction, and endocrine function. To better understand the dynamic changes occurring during ovulation, our study has created an integrated scRNA-seq and iST resource that fully maps this landscape with resolution on the hour timescale. We developed an integrated framework that combines gene expression profiles from single-cell sequencing with spatial information to build a comprehensive map of ovarian cell types, what their functional programs are, and how these cells interact over the full course of ovulation.

Several studies have utilized single-cell methods to investigate ovarian biology, such as a single-cell ovary atlas across the mouse estrous cycle[18], single cells selected across follicle activation[19], and, recently, in premenopausal adult human samples[15,28,29]. These studies have been instrumental in delineating cell types in the ovary but have focused on specific regions of interest using GeoMX or provided deconvolved cell states during ovulation which lacks single-cell resolution[23,29]. Therefore, our study is unique in its distinctive focus on the temporal dynamics of ovulation across a short time frame, employing both scRNA-seq and iST, with true single-cell resolution, to enable data integration across both datasets. Here, we show successful integration of both data types allowing for inference of spatial expression of over 25,000 genes across the time course of ovulation. With this resource, we interrogated the transcriptional dynamics of ovulation, identified novel gene markers for ovulation-dependent cell types, revealed new biological pathways that may contribute to normal ovarian function, and uncovered novel CCIs that may be important for orchestrating these processes.

First, we identified all expected major cell types of the ovary, including cumulus cells, endothelial cells, epithelial cells, granulosa cells, luteal cells, myeloid cells, stromal cells, theca cells, and oocytes. It is likely that the majority of oocytes were filtered out during single-cell preparation suspension, and immature oocytes may have passed through the filter due to their smaller size[119]. We additionally identify time-dependent cell states, between which gene expression profiles were distinct enough to cause these cell states to cluster separately and be enriched for distinct functions and pathways. Our data revealed “early” and “late” subclusters of major ovarian cell types and our results demonstrate that early and late cell clusters can be broadly distinguished by shifts in their functional pathways, where there is a greater diversity of pathway terms in the clusters associated with the later timepoint in ovulation. Notably, we did not find any time-varying subclusters in myeloid and epithelial cells, which aligns with previous studies evaluating the mouse estrous cycle[20].

Although other transcriptomic investigations in the mouse ovary have identified time-dependent granulosa subclusters across the estrous cycle, such as the prevalence of mural cells in the estrus phase[18], the design of our study afforded increased resolution into granulosa cell types and states. Notably, we observed two time-varying cumulus cell subclusters whereas previous studies found cumulus cells to be clustered together with granulosa cells from preantral follicles or only one cumulus cell cluster across the ovulation time course. These differences may be driven by an increased number of cumulus cells present in our dataset, whether through our hyperstimulated mouse model versus ovulatory follicles naturally found during the estrous cycle, or a higher number of ovaries per timepoint[18,23]. Notably, the gene signature of the previously identified cumulus cell cluster aligns with our late cumulus cluster (Cumulus 2)[18]. As such, the identification of the early cumulus subcluster (Cumulus 1), which is uniquely enriched for neuronal pathways, may provide additional insight into its function and role in the preovulatory follicle. The detection of time-

dependent cumulus cell clusters also has unique relevance for non-hormonal contraceptive discovery as actively expanding cumulus cells are specific to ovulation.

We further investigated the enriched gene pathways and cell-cell interactions that contributed to the time-dependent changes in ovarian cell states during ovulation. Our findings of upregulated ECM genes and pathways in the Stroma 1 cluster, such as *Dcn and Ogn*, indicate that early stroma cells are primarily involved in ECM formation and maintenance of the tissue architecture as expected from previous literature[120,121]. In contrast, late stromal cells exhibit a variety of pathways including EGF signaling, angiogenesis, and hormone production, supporting a more diverse role for stromal cells in ovulation. Following the LH surge, EGFR signaling is critical for the ovulatory response across ovarian cell types, including stromal vasculature[122,123]. Although hormone biosynthesis is not a classic function of stroma cells, subpopulations of stroma cells capable of producing hormones have been documented in several species[124-129]. In theca cells, we identified two populations at the 0hr timepoint with one enriched for ovulation genes, such as *Fshr*, *Inhba*, and *Fst*, and another enriched with steroidogenesis, such as *Cyp17a1*. However, later theca subclusters transitioned towards enrichment of pathways involved with signal transduction, immune processes, and metal homeostasis. Similar to stromal cells, late theca subclusters, especially those at the 4hr timepoint, were highly enriched for EGFR signaling as expected following the LH surge[122,123]. Late theca cells also upregulated several immune processes, which aligns with its known role in cytokine production and leukocyte recruitment during ovulation[1]. A new insight from our data is the possible role of metal homeostasis in the functions of theca cells. In addition to steroid hormone production, the mitochondria also participate in metal homeostasis by taking in metals and chemically bonding them to proteins (metalation)[130,131.] As steroidogenesis generates reactive oxygen proteins, metalloproteins in theca cells may be involved in reducing reactive oxygen species. Taken together, our results reveal dynamic populations of stromal and theca cells and suggest several understudied functions for these cells during later time points in ovulation.

In luteal cells, we observed a shift in the nature of enriched pathways from early to late luteal cell subclusters. Mixed luteal cells, which include those from previous cycles, exhibited upregulation in lipid metabolism which aligns with the highly steroidogenic nature of luteal cells in mature corpus lutea[132]. Complementary to this function include enriched pathways in mitochondrial function, including redox homeostasis and ETC processes. Interestingly, mature corpus lutea exhibit increased mitochondrial volume and ATPase signal, suggesting that these novel pathways increase respiratory activity to support corpus luteum function. In Recent Luteal cells that are mainly present at 12hr, we observed upregulation in ECM and smooth muscle pathways. During this timepoint, luteal cells (composed of luteinized theca and granulosa cells) contribute to ECM remodeling for the formation of new corpus lutea[133]. This observation is further supported by the observed cell-cell interactions between theca or granulosa cells (senders) and luteal cells (receiver) at 12hr. Specifically, we found enriched interactions that promote tissue remodeling (*Timp1-Mmp2*) and angiogenesis (*Ang-Egfr*). In cumulus cells, we observed strikingly different pathways enriched when comparing the early and late subclusters. Notably, the early cumulus subcluster upregulated pathways relating to nervous system function. Since cumulus cells undergo substantial cellular changes during the LH surge, such as cell migration and retraction of transzonal projections from the oocyte, they may possess neural-like plasticity during expansion[134-137]. However, further evidence is required to elucidate the mechanisms of neuronal pathway genes during ovulation. In contrast, the late cumulus subcluster was enriched with primarily cholesterol metabolism pathways. Recent interactome analyses performed between cumulus and mural granulosa cells as senders and receivers, respectively, revealed a number of interactions related to steroidogenesis[100]. In addition, cumulus cells have been shown to produce progesterone that may partially serve as a sperm chemoattractant following ovulation[138].

Understanding the spatiotemporal expression of genes in the ovary throughout ovulation has a wide range of implications for infertility and non-hormonal contraceptive development. For example, one condition of particular relevance to this study is luteinized unruptured follicle (LUF) syndrome, in which follicle rupture and COC release do not occur but luteinization and progesterone secretion are maintained[139-141]. The cause of LUF syndrome is largely unknown, but LUFs are found in about 11% of women with regular menstrual cycles and up to 43% of women with infertility, with recurrence rates of up to 90% between cycles[142,143]. Because LUF syndrome does not impact hormone secretion, the genes dysregulated in this process may also serve as nascent ovulation-blocking targets that do not affect luteinization. Our study has revealed genes with significant changes in expression within non-luteinizing cells (e.g. cumulus cells) that may be important for orchestrating the morphological and transcriptomic changes that occur within a time span of hours to promote successful ovulation. Thus, this study has the capacity to isolate genes that regulate other key processes in ovulation beyond luteinization, such as COC expansion or follicle rupture, that may drive phenotypes like LUF and be harnessed as non-hormonal contraceptives. Taken together, our integrated dataset presents an array of possible contraceptive or fertility-based targets, representing a large and important resource for the field.

In summary, this study outlines the dynamic spatiotemporal profile of mouse ovaries across the ovulation time course by combining single-cell resolution with spatial localization. We identified time-varying cell subclusters for major ovarian cell types with enrichment of established and novel markers. Furthermore, we conducted cell-cell interaction analyses between ovarian cell types throughout ovulation, which revealed previously undescribed ligand-receptor interactions. This comprehensive dataset provides the framework to further investigate ovarian cell states during ovulation and may provide implications to better understand anovulatory conditions and drive the discovery of new contraceptive targets for women.

Limitations of the Study

In order to induce ovulation and maximize cell yield, mice were hyperstimulated with PMSG and hCG prior to ovary collection. It is possible that hyperstimulation may impact cell behavior to a different extent than what would occur in a natural ovulation cycle. In addition, because physiologic ovulation in mice occurs overnight, we offset induction of ovulation by 24h so that the single cell dissociations could be immediately processed within working hours of the sequencing core. However, we saw no difference in the number of COCs ovulated with the natural or offset ovulation timing (**Figure S2B**) and confirmed that ovulation occurred as expected via histology (**Figure S1**).

Spatial transcriptomics as a novel technology still has various limitations. Cell segmentation is challenging due to the intricate and densely packed cellular environments, which can often lead to false positives and negatives in identifying and distinguishing individual cells. Additionally, the manual selection of probes and the limit to the number of probes restricts our ability to capture a more unbiased spatial profile. On the other hand, single-cell RNA sequencing failed to detect a substantial number of oocytes because the dissociation method was inefficient at capturing larger cells, leading to an underrepresentation of this cell type.

Acknowledgements

We would like to thank Hoi Chang Lee and Yiru Zhu for their assistance in collecting the ovary samples utilized in this study, and Elizabeth Tsui for providing a protocol for dissociation of single cells from the ovary that we adapted for this study. We also thank the Northwestern University Sequencing Core for conducting the single-cell sequencing of our samples. This work is supported by the Bill & Melinda Gates Foundation (INV-00385 to F.E.D., B.A.G., and A.K.S.) and National Institutes of Health (U01 MH130962 and RF1 MH121289 to S.L.F. and B.C.). C.E.K. is supported in part by was supported by Eunice Kennedy Shriver National Institute of Child Health and Human Development of the National Institutes of Health under Award Number T32HD094699.

B.A.G. is supported in part by the Geisel School of Medicine at Dartmouth's Center for Quantitative Biology through a grant from the National Institute of General Medical Sciences (NIGMS, P20GM130454) of the NIH. The content is solely the responsibility of the authors and does not necessarily represent the official views of the National Institutes of Health.

Author Contributions

Conceptualization, F.E.D and B.A.G.; Methodology, R.H., C.E.K., C.M., L.T.Z., S.L.F., F.E.D, S.L.F., A.K.S., and B.A.G.; Software, R.H., J.P.B., and B.C.; Validation, R.H., and C.E.K.; Formal Analysis, R.H., C.E.K., and J.P.; Investigation, R.H., C.E.K., E.Z., C.M., D.D.R., and J.N.; Resources, A.K.S. and S.L.F.; Data curation, R.H., Manuscript preparation, B.A.G., F.E.D, R.H., C.E.K., and J.P.B.; Manuscript Review & Editing, all authors; Visualization, B.A.G, F.E.D., R.H., C.E.K., J.P.B.; Supervision, A.K.S., B.A.G. and F.E.D.; Project Administration, J.P, A.K.S., S.L.F., F.E.D., and B.A.G.; Funding Acquisition, A.K.S, S.L.F., B.C., F.E.D, and B.A.G.

Declarations of Interests

A.K.S. reports compensation for consulting and/or SAB membership from Honeycomb Biotechnologies, Cellarity, Repertoire Immune Medicines, Ochre Bio, Relation Therapeutics, Bio-Rad Laboratories, Passkey Therapeutics, Fog Pharma, Dahlia Biosciences, and intrECate Biotherapeutics unrelated to this work. B.A.G., R.H., C.E.K., Y.Z., S.L.F., C.M., A.K.S., F.E.D., H.C.L., L.T.Z., E.Z., and J.N. have filed a patent related to the work described in this study (patent application no. PCT/US24/25824).

Figure Legends

Figure 1. Single-cell and spatial transcriptomic analysis of adult mouse ovaries throughout the time course of ovulation. (A) Schematic depicts the workflow for single cell and spatial transcriptomic analyses. Mice were hyperstimulated with PMSG and hCG and ovaries were dissected 0hr, 4hr, or 12hr post-hCG injection, processed, and submitted for scRNA-seq or MERFISH analysis. **(B)** UMAP shows all 16 identified cell type clusters. The cell counts for each cluster were as follows: Cumulus 1 = 2910, Cumulus 2 = 908, Endothelial 1 = 891, Endothelial 2 = 212, Epithelial = 440, Granulosa 1= 2931, Granulosa 2 = 1781, Granulosa 3 = 3044, Luteal 1 = 1421, Luteal 2 = 2641, Myeloid = 816, Oocyte = 16, Stroma 1 = 2042, Stroma 2 = 2970, Theca 1 = 1051, Theca 2 = 1640. **(C)** Heatmap shows five marker genes used to determine the identity of each cell cluster. **(D)** Stacked bar plot showing the percent of cells in each cluster expressed at each time point. **(E)** Pie charts showing the categorization of pathways upregulated in early (0h) vs. late (12h) timepoints. **(F)** Examples of 0hr, 4hr, and 12hr MERFISH ovary sections with seven major cell types localized. The remaining ovaries can be visualized in Figure S4B.

Figure 2. Stroma cells exhibit time-dependent changes in gene expression. (A) UMAP shows the clustering of stroma cells from scRNA-seq data. A stacked bar plot shows the percent of cells in stromal clusters expressed at each time point. **(B)** Heatmap depicts differential gene expression in Stroma 1 (early) and Stroma 2 (late) clusters from scRNA-seq data. **(C)** Inferred expression of Dcn from the integration of scRNA-seq and iST data shows localization to stroma cells. (**D**) Expression plot of Pdgfra from iST data shows localization to stroma cells. (**E**) Same with C but with *Egflam.* (**F**) Same with C but with *Pdzrn3*. **(G)** Dot plots show top processes upregulated in Stroma 1 (left) and Stroma 2 (right).

Figure 3. Theca cells exhibit time-dependent changes in gene expression. (A) UMAP shows the clustering of theca cells at the top-level (dotted line) and the subcluster level (dots) from scRNA-seq data. A stacked bar plot shows the percent in theca subclusters expressed at each time point. **(B)** Heatmap depicts differential gene expression in Theca 1 (early) and Theca 2 (late) clusters from scRNA-seq data. **(C)** Expression plot of *Cyp17a1* from iST data shows localization to theca cells. (**D**) Inferred expression of *Col4a1* from the integration of scRNA-seq and iST data shows localization to theca cells. (**E**) Same with D but with *Oca2.* (**F**) Same with D but with *Fam161a*. **(G)** Dot plots showing top processes upregulated in Theca 0hr_1 (top left), Theca 0hr_2 (top right), Theca 4hr (bottom left), and Theca 12hr (bottom right).

Figure 4. Luteal cells exhibit time-dependent changes in gene expression. (A) UMAP shows the clustering of luteal cells at the top-level (dotted line) and the subcluster level (dots) from scRNA-seq. A stacked bar plot shows the percent of cells in luteal subclusters expressed at each time point. **(B)** Heatmap depicts differential gene expression in Recent Luteal and Mixed Luteal sub-clusters from scRNA-seq. (**C**) Expression plot of *Lhcgr* from iST data shows localization to luteal cells. (**D**) Same with C but with *Runx1.* **(E)** Same with C but with *Gm2a.* (**F**) Inferred expression of *Fndc3b* from the integration of scRNA-seq and iST data shows

localization to stroma cells. **(G)** Dot plots show top processes upregulated in Mixed Luteal (top left), Other Luteal (top right), Recent Luteal (bottom right), and Mural Luteal (bottom left) subclusters.

Figure 5. Cumulus cells exhibit time-dependent changes in gene expression. (A) UMAP shows the clustering of cumulus cells from scRNA-seq. A stacked bar plot shows the percent of cells in cumulus clusters expressed at each time point. **(B)** Heatmap depicting differential gene expression in Cumulus 1 (early) and Cumulus 2 (late) clusters from scRNA-seq. **(C-F)** RNAscope images show RNA expression of cumulus cell genes of interest, including (**C**) *Sult1e1*, (**D**) *Lox*, (**E**) *Zpf804a*, and (**F**) *Emb.* Top: Ovary scans at 20x magnification. Middle: Brightfield images of COCs at 40x magnification. Bottom row: Deconvoluted images of COCs at 40x magnification. **(G)** Dot plots show top processes upregulated in early (left) and late (right) cumulus cells.

Figure 6. Cell-cell interactions between cell types change throughout ovulation. (A) Circle plots show the change of interactions between various cell types at different time points. **(B)** Scatterplot shows incoming interaction strength and outgoing interaction strength for all cell types present within the 0hr (left), 4hr (middle), and 12hr (right) timepoints. **(C)** Dot plots show scaled interaction strength between granulosa cells and cumulus cells with upregulated interactions centered at 0hr (top) and 4hr (bottom). **(D)** Dot plots show scaled interaction strength between stroma cells and luteal cells with upregulated interactions centered at 0hr (top), 4hr (middle), and 12hr (bottom). **(E)** Dot plots show scaled interaction strength between theca cells and luteal cells with upregulated interactions centered at 0hr (top), 4hr (middle), and 12hr (bottom). **(F)** Dot plots show scaled interaction strength between granulosa cells and luteal cells with upregulated interactions centered at 0hr (top), 4hr (middle), and 12hr (bottom). **(G-I)** Expression plots show colocalization of (**G**) *Lama2* and *Itga9* (0hr), (**H**) *Fgf2* and *Sdc3* (4hr), and (**I**) *Fgf2* and *Sdc4* (12hr).

Supplemental Figure Legends

Supplementary Figure S1. H&E-stained sections of ovaries collected during in vivo ovulation time course, related to Figure 1. Examples of ovaries collected **(A)** 0hr, **(B)** 4hr, or **(C)** 12hr post hCG injection (left) and insets labeling key cell types (right). O = oocyte, CC = cumulus cells, GC = granulosa cells, TC = theca cells, SC = stroma cells, LC = luteal cells, Epi = epithelial cells. Scale bars = 200 µm.

Supplementary Figure S2. Schematic of optimization protocols for ovary collection (A-B) and MERFISH (C-D), related to Figure 1 and STAR methods. (A) Table depicting timing of hormone (PMSG and hCG) injections and ovary collection in control and offset timing groups. **(B)** Graph showing the average number of COCs collected per mouse in control and offset timing groups. **(C)** Top row: Pregnant mare serum gonadotropin (PMSG) and human chorionic gonadotropin (hCG)-stimulated, flash-frozen mouse ovaries were collected as intact whole ovaries or contralaterally-halved ovaries. Samples were embedded into a pre-formed OCT tissue microarray scaffold (TMA) with the ovarian hilums (indicated by red asterisk *) pointing downward towards the tissue microarray base, enabling uniform tissue section collection onto fluorescent microsphere-coated functionalized coverslips. Bottom row: corresponding images of bisected ovaries, embedding into the TMA scaffold, and 10x DAPI imaging of the resulting tissue sections. **(D)** MERFISH protocol of mounted samples undergoing a series of staining and incubations (fixation, permeabilization, hybridization, polyacrylamide gel embedding, tissue clearing with detergents).

Supplementary Figure S3. Quality Checks, related to Figure 1. **(A-B)** Quality metrics for spatial transcriptomics dataset: bar plots on number of transcripts per cell and cell volume post-filtering. **(C)** UMAP of the single-cell dataset, including unknown clusters. **(D)** Quality metrics for single-cell dataset: Violin plots on genes per cell and percent mitochondrial in the single-cell dataset post-filtering. **(E)** Clustered dot plot compares cell types found in both datasets using established markers.

Supplementary Figure S4. Clustering and cell identification of spatial transcriptomic dataset, related to Figure 1. (A) Expression plots of known markers for cell types identified in all ovaries at three time points show corresponding localization. **(B)** Ovaries serve as biological replicates that are not included in the main figures, colored by cell types identified. **(C)** Heatmap showing three top marker genes used to determine the identity of each cell cluster for each ovary in iST.

Supplementary Figure S5. Integration analysis of single-cell and spatial transcriptomics, related to Figure 1 and STAR methods. (A) Bar plots of training scores for training genes (left) and scatter plot of test scores vs sparsity for test genes (right), for the three integrations at 0hr (top), 4hr (middle), and 12hr (bottom). **(B)** Expression plots of *Col1a2* for predicted and observed results show similar patterns. **(C)** RNAscope

images (left) and predicted results from integration analysis (right) show similar expression patterns. Scale bars = 200 µm.

Supplementary Figure S6. Outgoing and incoming cell-cell interactions, related to Figure 6. (A) Bar plot of total number of interactions per ovulation time point. **(B)** Heatmap of incoming and outgoing signal patterns at the 0hr timepoint. **(C)** Heatmap of incoming and outgoing signal patterns at the 4hr timepoint. **(D)** Heatmap of incoming and outgoing signal patterns at the 12hr timepoint. **(E-G)** Expression plots show colocalization of the whole ovary for **(E)** *Lama2* and *Itga9* (0hr), **(F)** *Fgf2* and *Sdc3* (4hr), and **(G)** *Fgf2* and *Sdc4* (12hr).

STAR ⍰ Methods

Key resources table

REAGENT or RESOURCE	SOURCE	IDENTIFIER
Chemicals, peptides, and recombinant proteins		
Collagenase IV	Sigma-Aldrich	Cat#C5138
Harris hematoxylin	EK Industries	Cat#4797
Eosin Y	Thomas Scientific	Cat#C310Q20
Modified Davidson's	Electron Microscopy Services	Cat#64133-50
Pregnant mare serum gonadotropin	ProSpec Bio	Cat#HOR-272
Human chorionic gonadotropin	Sigma-Aldrich	Cat#C1063
Dulbecco's phosphate-buffered saline, no calcium, no magnesium	Fisher Scientific	Cat#14190-144
Dulbecco's phosphate-buffered saline, calcium, magnesium	Fisher Scientific	Cat#14040-133
Minimum Essential Media α Glutamax™, no nucleosides	Thermo Fisher Scientific	Cat#32561-037
Bovine serum albumin	Sigma-Aldrich	Cat#A3311
1x insulin-transferrin-selenium	Sigma-Aldrich	Cat#1884
Liberase DH	Sigma-Aldrich	Cat#05401089001
DNAse I	Sigma-Aldrich	Cat#9003-98-9
Red blood cell lysis solution	Miltenyi Biotec	Cat#130-107-677
Fetal bovine serum	Thermo Fisher Scientific	Cat#10082139
Critical commercial assays		
RNAscope 2.5 HD Reagent Kit—RED	ACD	Cat#322350
Chromium Next GEM Single Cell 3' Reagent Kits v3.1	10X Genomics	Cat#PN-1000286
Dual Index Kit TT Set A	10X Genomics	Cat#PN-1000215
MERSCOPE Cell Boundary Staining Kit	Vizgen	Cat#PN-10400009
MERSCOPE 140 Gene Imaging Kit, 1 sample	Vizgen	Cat#PN-10400004
Deposited data		
Single cell dataset of the mouse	This paper	

ovary throughout the time course of ovulation		
Spatial transcriptomic dataset of the mouse ovary throughout the time course of ovulation	This paper	
Experimental models: Organisms and strains		
Mouse: CD1	Inotiv	Cat#030
Oligonucleotides		
RNAscope probe Sult1e1	ACD	Cat#900181
RNAscope probe Zfp804a	ACD	Cat#1161171-C1
RNAscope probe Emb	ACD	Cat#462011
RNAscope probe Lox	ACD	Cat#425311
RNAscope probe Trpv4	ACD	Cat#406071
RNAscope probe Sik3	ACD	Cat#526431
RNAscope probe Slc6a6	ACD	Cat#544751
RNAscope Positive Control probe PPib	ACD	Cat#313911
RNAscope Negative Control probe Dapb	ACD	Cat#310043
Software and algorithms		
Cellranger	10x Genomics	https://support.10xgenomics.com/single-cell-gene-expression/software/overview/welcome
Seurat	Hao et al.[25]	https://cran.r-project.org/web/packages/Seurat/index.html
NicheNet	Browaeys et al.[147]	https://github.com/saeyslab/nichenetr
Squidpy	Palla et al.[155]	https://github.com/scverse/squidpy
Tangram	Biancalani et al.[26]	https://github.com/broadinstitute/Tangram
MAST	Finak et al.[145]	https://github.com/RGLab/MAST
DEseq2	Love et al.	https://github.com/thelovelab/DESeq2
Scanpy	Wolf et al.[154]	https://github.com/scverse/scanpy
Enrichr	Kuleshov et al.[151]	https://github.com/wjawaid/enrichR
CellChatDB	Jin et al.[146]	www.cellchat.org/cellchatdb
MultiNicheNet	Browaeys et al.[147]	https://github.com/saeyslab/multinichenetr
DoubletFinder	McGinnis et al.[144]	https://github.com/chris-mcginnis-ucsf/DoubletFinder
CellPose	Stringer et al.[153]	https://github.com/MouseLand/cellpose
MERlin	Emanuel et al.[152]	https://github.com/emanuega/merli

		n
Fiji	Schindelin et al.[157]	https://github.com/fiji; RRID:SCR_002285
Original code used to perform scRNAseq and spatial transcriptomic analyses	This paper	

Resource availability

Lead contact

Further information and requests for resources and reagents should be directed to and will be fulfilled by the lead contact, Brittany A. Goods (britt.anne.goods@dartmouth.edu).

Materials availability

This study did not generate new unique reagents.

Data and code availability

Cell-level data and gene-level data will be made available at the time of final publication. All code used in this manuscript for data processing and analysis will be made available on GitHub prior to final publication.

Experimental model and study participant details:

Animals

Female CD1 mice were purchased from Inotiv (West Lafayette, IN, USA) and used when reproductively adult (6-12 weeks). Mice were housed in the Center for Comparative Medicine at Northwestern University within a controlled barrier facility (Chicago, IL, USA) and kept at a constant temperature and humidity in a light cycle of 14hr light and 10hr dark. Mice were provided with food and water ad libitum and fed a specific chow that excludes soybean meal (Teklad Global 2916 chow, Envigo, Indianapolis, IN, USA). The Institutional Animal Care and Use Committee at Northwestern University approved all animal experiments, which were also performed in accordance with the National Institute of Health Guide for the Care and Use of Laboratory Animals.

Method details:

Optimization of ovulation timing for workflow compatibility

Physiological ovulation in mice typically occurs in the middle of the night which precludes necessary sample processing during normal operating hours of the NU Sequencing core. Therefore, we determined whether we could offset the timing of ovulation in mice by 12hr without affecting egg yield. Mice were hyperstimulated with pregnant mare serum gonadotropin (PMSG; ProSpec, #HOR-272) 12hr apart to stimulate follicle growth. Mice were then injected with human chorionic gonadotropin (hCG; Sigma Aldrich, #C1063) 46hr after relative PMSG injections to induce ovulation, and 14hr post-hCG injection, ovulated COCs were collected from the oviduct. COCs were denuded of cumulus cells, and the number of MII eggs was compared between the control and

offset groups (**Figure S2A and S2B**). Similar egg numbers were collected across groups demonstrating that ovulation was not impacted by this shift in superovulation timing.

Generation of single-cell suspensions from mouse ovaries

Ovulation induction was offset by 12hr as described above for this experiment. As detailed in **Figure 1A**, mice received an intraperitoneal injection of 5 I.U. PMSG to stimulate follicle growth. A second intraperitoneal injection of 5 I.U. hCG was given 46h following PMSG injection to induce ovulation. Ovary dissection occurred 0, 4, or 12hr post-hCG injection, with two independent operators dissecting ovaries from 3 mice each. One ovary from each mouse was pooled for single-cell isolation, with a total of three ovaries per suspension (labeled ABC or DEF). The contralateral ovary of each mouse was used for MERSCOPE analysis (see below).

The pooled ovaries were cut into quarters using insulin syringe needles and enzymatically digested in 2 mL aMEM-Glutamax supplemented with 1 mg/mL bovine serum albumin (BSA; Sigma-Aldrich, #A3311) and 1x insulin-transferrin-selenium (Sigma-Aldrich, #1884) containing 40 µg/L liberase DH (Sigma-Aldrich, #05401089001), 0.4mg/mL collagenase IV (Sigma-Aldrich, #C5138), and 0.2 mg/mL DNAse I (Sigma-Aldrich, #9003-98-9) for 15 minutes with gently agitation at 37°^{C} and 5% CO_2 for 15 minutes. Ovaries were then mechanically digested via trituration using a 1000P wide bore tip, and the suspension was strained through a pre-wet 30 µm strainer directly into aMEM-Glutamax containing 10% FBS to quench the enzymes. Any remaining pieces of ovary were returned to the incubator in 2 mL fresh digestion media for another 15 minutes, followed by repeat mechanical digestion and straining. Once the enzymatic and mechanical digestions were complete, the cell suspension was centrifuged at 300g for 10 minutes at 4□. The supernatant was removed, and the remaining cell pellet was resuspended in 100 µL Red Blood Cell Lysis solution (Miltenyi Biotec, #130-107-677) and incubated for 10 min at 4°C. After red blood cell removal, the suspension was centrifuged again at 300g for 10 minutes at 4°C. Following supernatant removal, the resulting pellet was resuspended in 100µL of 0.025% BSA in phosphate-buffered saline without calcium or magnesium, and transferred to lo-bind Eppendorf tubes. The suspension was placed on ice and transferred immediately to the Northwestern University Sequencing Core (Chicago, IL, USA).

Single-Cell Library Preparation and Sequencing

Cell number and viability were analyzed using Nexcelom Cellometer Auto2000 with AOPI fluorescent staining method. Sixteen thousand cells were loaded into the Chromium iX Controller (10X Genomics, PN-1000328) on a Chromium Next GEM Chip G (10X Genomics, PN-1000120), and processed to generate single-cell gel beads in the emulsion (GEM) according to the manufacturer's protocol. The cDNA and library were generated using the Chromium Next GEM Single Cell 3' Reagent Kits v3.1 (10X Genomics, PN-1000286) and Dual Index Kit TT Set A (10X Genomics, PN-1000215) according to the manufacturer's manual. Quality control for the constructed library was performed by Agilent Bioanalyzer High Sensitivity DNA kit (Agilent Technologies, 5067-4626) and Qubit DNA HS assay kit for qualitative and quantitative analysis, respectively. The multiplexed libraries were pooled and sequenced on Illumina Novaseq6000 sequencer with 100 cycle kits using the following read length: 28 bp Read1 for cell barcode and UMI, and 90 bp Read2 for transcript. The single-cell library preparation and sequencing were performed at the Northwestern University NUseq core facility with the support of an NIH Grant (1S10OD025120).

Single-cell RNA-seq (scRNAseq) Analysis

Raw sequencing data was demultiplexed using Cell Ranger from 10x Genomics, converting the raw data into FASTQ format. Cell Ranger was also used for the alignment of the FASTQ files to the reference genome and

counting the number of reads from each cell that aligned to each gene. R version 4.2.2 and Seurat version 4 were used for all downstream analyses unless specified otherwise[25]. For initial quality filtering, cells with greater than 20% mitochondrial gene expression (percent.mt) and less than 3000 expression counts (n_FeatureRNA) were removed. The data did not show any significant batch effects. Standard Seurat pipelines were used to scale, find variables, and normalize the dataset. The identified list of variable genes was used to perform the principal component analysis. Cell clusters were identified with the Find-Neighbors function with dims = 1:20 and the FindClusters function with resolution = 0.5. Subclusters were found with iterative clustering with different resolutions of 0.5, 0.1, and 0.3. DoubletFinder_v3 was used to remove doublets with an approximate 5% expected ratio[144]. MAST was used to perform all differential expression analyses[145]. Cell-cell interaction analysis was performed with CellChatDB and Multinichenet packages[146,147].

Gene Ontology Analysis

The online knowledgebase published by the Gene Ontology Consortium (GO Enrichment Analysis Tool), and several gene set enrichment analysis tools available via Enrichr (Reactome 2022, KEGG 2021 Human, GO Biological Process 2023) were utilized to perform GO analyses on each cell cluster[148-151]. Gene IDs for the top 150 genes upregulated in each cluster were inputted into each tool. For the GO Enrichment Analysis Tool, “biological process” and “mus musculus” were selected as search filters. GO results from Enrichr and the GO Enrichment Analysis Tool were sorted by ascending adjusted p-value and descending fold enrichment, respectively, and only pathways with adjusted p-values< 0.05 were included in the analysis. Pathways highlighted in this study were selected from the top ten pathways from Enrichr or the GO Enrichment Analysis Tool. Selected pathways were annotated by category based on the biological function consistent with the pathway and cell type.

Preparation of ovaries and microarray assembly for Multiplexed Error-Robust Fluorescence in situ Hybridization (MERSCOPE) analysis

Ovaries intended for MERSCOPE analysis were collected in RNAse-sterile conditions as intact whole ovaries and stored in cryo-safe tubes and flash frozen in liquid nitrogen before shipping to the Broad Institute for TMA construction and MERSCOPE processing (**Figure S2C**). In RNAse-sterile conditions, samples were embedded and frozen in a pre-formed scaffold of Optimal Cutting Temperature media, oriented so that the ovarian hilum was at the base of the microarray and stored at -80°C until sectioning. The ovaries were assembled in this tissue-microarray (TMA) as three whole ovaries per each timepoint (0hr, 4hr, and 12hr) for a total of 9 ovaries. 10µm-thick sections of the TMA were obtained using a cryostat at -20°C, mounted on fluorescent microsphere-coated, functionalized coverslips, fixed in 4% PFA in 1X PBS, and permeabilized in 70% ethanol overnight (**Figure S2D**).

Following permeabilization in 70% ethanol, the TMA section was stained with Vizgen’s Cell Boundary Stain Kit (PN 10400009). The section was washed briefly with 1X PBS before being incubated for 1hr and room temperature in 100µL of Cell Boundary Blocking Buffer Premix (PN 20300012) and 5µL of murine RNase inhibitor, with a 2x2cm square of parafilm over the sample to spread the mixture and prevent drying. The section was then incubated for another hour at room temperature in a mixture of 100µL Cell Boundary Blocking Buffer, 5µL RNase inhibitor, and 1µL of Cell Boundary Primary Stain Mix (PN 20300010) with parafilm as described above. The section was washed three times with 5ml 1X PBS on a rocker before a final 1-hr incubation at room temperature in 100µL Cell Boundary Blocking Buffer Premix, 5µL RNase inhibitor, and 3µL Cell Boundary Secondary Stain Mix (PN 20300011) with parafilm as described above. The section was washed three times with 5ml 1X PBS on a rocker at room temperature, then fixed again in 4ml of 4% PFA in

1X PBS, followed by two 5ml 1X PBS, all at room temperature. To hybridize the MERSCOPE probes to the section, the sample was first briefly washed in 2X saline-sodium citrate (SSC) at room temperature, and incubated in 30% formamide in 2X SSC at 37°C for 30 minutes. 50µL of the probe mixture and 1µL of RNase inhibitor were added on top of the sample and covered with parafilm as described above, and the section was incubated for 48h at 37°C. After two 30 minute incubations at 37°C in 30% formamide in 2X SSC, the sample embedded in a polyacrylamide gel solution (3.9ml nuclease-free water, 0.5ml 40% acrylamide/bis solution 19:1, 0.3ml 5M NaCl, 0.3ml Tris pH8, 25µL 10% w/v ammonium persulfate in nuclease-free water, 2.5ul of N,N,N',N'-tetramethylethylenediamine). To embed the section, excess formamide was first removed with a 2-minute incubation of 2X SSC while the gel mixture was prepared. Once the gel was prepared, the sample was incubated in 5ml of the gel mixture for one minute. Then the sample was transferred to a clean petri dish, the excess gel mixture was wicked away with a Kimwipe, and 50µL of reserved gel mixture was added on top of the section. A 20mm glass coverslip that was cleaned and treated with 50µL of GelSlick was inverted on top of the sample, spreading out the gel evenly. The excess gel mixture was wicked away with a Kimwipe, and the sample was left at room temperature for 2hr while the gel was set. To clear excess proteins from the sample, the 20mm coverslip was removed after the gel had completely set, and the sample was incubated in 5ml of clearing mixture (3.4ml nuclease-free water, 1ml 10% sodium dodecyl sulfate (SDS), 0.5ml 20X SSC, and 0.1ml 25% Triton-X) for 3 days at 37°C.

Selection of MERSCOPE Genes

A MERSCOPE panel of 198 genes consisting of marker genes, genes known to be involved in ovulation, and additional genes-of-interest were constructed based on published literature or preliminary data from our lab and others. Marker genes were chosen to facilitate the identification of cell types including granulosa, luteal, germ, mesenchymal, endothelial, epithelial, and immune cells[18,19].

Construction of MERSCOPE probes

A fluorescently tagged oligo probe library for 198 combinatorial genes and 3 sequential genes was designed, with each probe encoding the barcodes assigned to specific target RNA transcripts in the library. RNA targets were selected based on increasing the success of probe binding and ensuring gene expression falls within optically appropriate parameters for MERSCOPE imaging. Manufacturing services occurred at Vizgen, Inc.

MERSCOPE Imaging

The cleared sample was briefly washed three times with 5ml of 2X SSC, stained with 3ml of Vizgen DAPI and PolyT Staining Reagent (PN 20300021) for 10 minutes on a rocker, incubated in 30% formamide in 2X SSC for fifteen minutes, and then transferred to 2X SSC while the MERSCOPE instrument was prepared. The MERSCOPE flow chamber was cleaned with RNaseZap™ RNase Decontamination Solution and 70% ethanol. A Vizgen MERSCOPE 300 Gene Imaging Cartridge (PN 20300017) was thawed and activated by adding 250µL of Vizgen Imaging Buffer Activator (PN 20300022) and 100µL of RNase inhibitor. 15ml of mineral oil was added on top of the imaging solution in the cartridge to prevent oxidation. The MERSCOPE was initialized, and primed, the section was loaded into the flow chamber, and the flow chamber was attached to the MERSCOPE fluidics system and wetted, checking for bubbles before proceeding. A 10X overview was first acquired of the entire imageable area, and regions of interest were selected before moving to the 60X, which was cleaned and oiled before acquiring the MERSCOPE images. Once imaging was complete, a cell boundary stain was selected for cell segmentation and image analysis was performed on the MERSCOPE using Vizgen's MERlin pipeline to acquire transcript count and cell segmentation data.

MERSCOPE Analysis

Cell segmentation was performed on the MERSCOPE using Vizgen's provided pipeline, which utilizes CellPose and MERlin to acquire cell and transcript data[152,153]. Python version 3.7.12 was used to perform all analysis unless specified otherwise. Cells with less than 10 transcript counts were removed. Scanpy was used to find the variables, normalize, scale, perform PCA, find neighborhoods, and cluster cells with Leiden[154]. To identify the cell type for each cluster, we counted the number of transcripts for each gene in every cluster and looked for known markers in the top 10. We also performed differential expression analysis using Seurat v3 in R to find markers for each Leiden cluster[25]. Squidpy along with anndata and scanpy was used to visualize the regions spatially[154,155]. Cell-cell interaction analysis was performed with CellPhoneDB[156].

MERSCOPE-10X Integration Analysis

Integration of MERSCOPE and 10X single-cell datasets was performed using the package Tangram[142]. Out of the 198 genes in the MERSCOPE gene probes, 18 test genes were randomly selected to be left out of the training process, including *Hmgcs2*, *Col1a2*, *Ly6e*, *Krt18*, *Nr2f2*, *Oca2*, *Sult1e1*, *Ccr7*, *Ptprc*, *Cd14*, *Wnt5a*, *Kitl*, *Pbk*, *Rasd1*, *Folr1*, *Rnd3*, *Mro*, and *Cldn5*, to later assess the performance of the integration. The learning model uses the leave-one-out validation strategy, where the remaining 180 genes were partitioned into 179 training genes and a single validation gene. The algorithm repeated the training 180 times, each time leaving out a different one, to obtain a prediction for each gene. The overall performance of the analysis is evaluated in three ways: 1) training and testing scores were obtained to quantify the deep learning model performance, 2) comparison of gene expression from those randomly selected from the test set between the MERSCOPE dataset and their predicted expression based on the integration algorithm, and 3) validation of predicted gene expression patterns from integrated algorithm with RNAscope images using genes not originally in the MERSCOPE probes.

Histological processing and staining

Immediately after collection, mouse ovaries were placed in tubes containing 1 mL Modified Davidson's solution (Electron Microscopy Services, Hatfield, PA) and rocked for 2-4hr at room temperature. Ovaries were then stored overnight at 4°C with gentle rocking. The next morning, ovaries were washed in 70% ethanol three times with 10 minutes per wash. Using standard processing protocols, an automated tissue processor (Leica Bioscystems. Buffalo Grove, IL) was used to process, dehydrate, and embed the ovaries in paraffin wax. Ovaries were then serially sectioned at 5-µm-thick intervals until the approximately half of the ovary was sectioned, and sections were placed on glass slides. The slide containing the approximate midsection of the ovary was stained with hematoxylin and eosin using a standard H&E staining protocol. Stained sections were cleared using 3 5-minute-incubations with Citrisolv (Decon Laboratories Inc., King of Prussia, PA) and then mounted with Cytoseal XYL (ThermoFisher Scientific).

RNA *in situ* hybridization

The expression of mouse *Sult1e1* (ACD, #900181), *Lox* (ACD, #425311), *Emb* (ACD, #462011), *Zfp804a* (ACD, #1161171-C1), *Trpv4* (ACD, #406071), *Sik3* (ACD, #526431), and *Slc6a6* (ACD, #544751) in whole ovary sections was detected using the RNAscope 2.5 HD Red Assay (Advanced Cell Diagnostics (ACD)). Samples were incubated with positive (*Ppib*; ACD, #313911) and negative (*Dapb*; ACD, #310043) control probes or target probes for 2h at 40°C and counterstained with hematoxylin and ammonia water. The EVOS FL Auto imaging system was used to scan whole ovary sections at 20x resolution and image COCs at 40x magnification. Images were then color deconvoluted using Fiji[157] to improve signal visibility. The full, step-wise

protocol for this assay can be found on the ACD website (https://acdbio.com/sites/default/files/322360-USM%20RNAscope%202.5%20HD%20RED%20Pt2_11052015.pdf)

Supplemental File Information

Excel file S1. Marker genes for top-level clusters, related to Figure 1
Excel file S2. Pathway analysis for top-level clusters, related to Figure 1
Excel file S3. Marker genes for subclusters, related to Figures 2-5
Excel file S4. Differentially expressed genes between time-dependent cell states, related to Figures 2-5
Excel file S5. Pathway analysis results for subclusters, related to Figures 2-5

References

1. Tan, O.L. and Fleming, J.S. (2004). Proliferating cell nuclear antigen immunoreactivity in the ovarian surface epithelium of mice of varying ages and total lifetime ovulation number following ovulation. Biol. Reprod. *71*, 1501–1507. 10.1095/biolreprod.104.030460.

2. Duffy, D.M., Ko, C., Jo, M., Brannstrom, M., and Curry, T.E. (2019). Ovulation: Parallels With Inflammatory Processes. Endocr. Rev. *40*, 369-416. 10.1210/er.2018-00075.

3. Marik, J. and Hulka, J. Luteinized unruptured follicle syndrome: a subtle cause of infertility. (1978). Fertil. Steril. *29*, 270-274. 10.1016/s0015-0282(16)43151-1.

4. Qublan, H., Amarin, Z., Nawasreh, M., Diab, F., Malkawi, S., Al-Ahmad, N., and Balawneh, M. (2006). Luteinized unruptured follicle syndrome: incidence and recurrence rate in infertile women with unexplained infertility undergoing intrauterine insemination. Hum. Reprod. *21*, 2110-2113. 10.1093/humrep/del113.

5. Wang, L., Qiao, J., Liu, P., and Lian, Y. (2008). Effect of luteinized unruptured follicle cycles on clinical outcomes of frozen thawed embryo transfer in Chinese women. J. Assist. Reprod. Genet. *25*, 229–233. 10.1007/s10815-008-9225-2.

6. Vandereyken, K., Sifrim, A., Thienpont, B. and Voet, T. (2023). Methods and applications for single-cell and spatial multi-omics. Nat. Rev. Genet. *24*, 494–515. 10.1038/s41576-023-00580-2.

7. Piwecka, M., Rajewsky, N. and Rybak-Wolf, A. (2023). Single-cell and spatial transcriptomics: deciphering brain complexity in health and disease. Nat. Rev. Neurol. *19*, 346–362. 10.1038/s41582-023-00809-y.

8. Yao, Z., van Velthoven, C.T.J., Kunst, M., Zhang, M., McMillen, D., Lee, C., Jung, W., Goldy, J., Abdelhak, A., Aitken, M., et al. (2023). A high-resolution transcriptomic and spatial atlas of cell types in

the whole mouse brain. Nature. *624*, 317-332. 10.1038/s41586-023-06812-z.

9. Wang, F., Long, J., Li, L., Wu, Z.X., Da, T.T., Wang, X.Q., Huang, C., Jiang, Y.H., Yao, X.Q., Ma, H.Q., et al. (2023). Single-cell and spatial transcriptome analysis reveals the cellular heterogeneity of liver metastatic colorectal cancer. Sci. Adv. *9*, eadf5464. 10.1126/sciadv.adf5464.

10. Baccin, C., Al-Sabah, J., Velten, L., Helbling, P.M., Grünschläger, F., Hernández-Malmierca, P., Nombela-Arrieta, C., Steinmetz, L.M., Trumpp, A., and Haas, S. (2020). Combined single-cell and spatial transcriptomics reveal the molecular, cellular and spatial bone marrow niche organization. Nat. Cell. Biol. *22*, 38-48. 10.1038/s41556-019-0439-6.

11. Fang, S., Chen, B., Zhang, Y., Sun, H., Liu, L., Liu, S., Li, Y., and Xu, X. (2023). Computational Approaches and Challenges in Spatial Transcriptomics. Genomics Proteomics Bioinformatics. *21*, 24-47. 10.1016/j.gpb.2022.10.001.

12. Liu, Z., Sun, D., and Wang, C. (2022). Evaluation of cell-cell interaction methods by integrating single-cell RNA sequencing data with spatial information. Genome Biol. *23*, 218. 10.1186/s13059-022-02783-y.

13. Piwecka, M., Rajewsky, N., and Rybak-Wolf, A. (2023). Single-cell and spatial transcriptomics: deciphering brain complexity in health and disease. Nat. Rev. Neurol. *19*, 346–362. 10.1038/s41582-023-00809-y.

14. Kanemaru, K., Cranley, J., Muraro, D., Miranda, A.M.A., Ho, S.Y., Wilbrey-Clark, A., Patrick Pett, J., Polanski, K., Richardson, L., Litvinukova, M., et al. (2023). Spatially resolved multiomics of human cardiac niches. Nature *619*, 801-810. 10.1038/s41586-023-06311-1.

15. Fan, X., Bialecka, M., Moustakas, I., Lam, E., Torrens-Juaneda, V., Borggreven, N.V., Trouw, L., Louwe, L.A., Pilgram, G.S.K., Mei, H., et al. (2019). Single-cell reconstruction of follicular remodeling in the human adult ovary. Nat. Commun. *10*, 3164. 10.1038/s41467-019-11036-9.

16. Park, C.J., Lin, P.C., Zhou, S., Barakat, R., Bashir, S.T., Choi, J.M., Cacioppo, J.A., Oakley, O.R., Duffy, D.M., Lydon, J.P., et al. Progesterone Receptor Serves the Ovary as a Trigger of Ovulation and a Terminator of Inflammation. (2020). Cell Rep. *31*, 107496. 10.1016/j.celrep.2020.03.060.

17. Li S., Chen L.N., Zhu H.J., Feng X., Xie F.Y., Luo S.M., Ou X.H., and Ma J.Y. (2021). Single-cell RNA sequencing analysis of mouse follicular somatic cells. Biol. Reprod. *105*, 1234-1245. 10.1093/biolre/ioab163.

18. Morris, M.E., Meinsohn, M.C., Chauvin, M., Saatcioglu, H.D., Kashiwagi, A., Sicher, N.A., Nguyen, N., Yuan, S., Stavely, R., Hyun, M., et al. (2022). A single-cell atlas of the cycling murine ovary. eLife *11*, e77239. 10.7554/eLife.77239.

19. Chen, Y.Y., Russo, D.D., Drake, R.S., Duncan, F.E., Shalek, A.K., Goods, B.A., and Woodruff, T.K. (2022). Single-cell transcriptomics of staged oocytes and somatic cells reveal novel regulators of follicle

activation. Reproduction *164*, 55–70. 10.1530/REP-22-0053.

20. Winkler, I., Tolkachov, A., Lammers, F., Lacour, P., Daugelaite, K., Schneider, N., Koch, M.L., Panten, J., Grünschläger, F., Poth, T., et al. (2024). The cycling and aging mouse female reproductive tract at single-cell resolution. Cell *187*, 981-998.e25. 10.1016/j.cell.2024.01.021.

21. Wamaitha, S.E., Nie, X., Pandolfi, E.C., Wang, X., Yang, Y., Stukenborg, J.B., Cairns, B.R., Guo, J., and Clark, A.T. (2023). Single-cell analysis of the developing human ovary defines distinct insights into ovarian somatic and germline progenitors. Dev. Cell *58*, 2097-2111.e3. 10.1016/j.devcel.2023.07.014.

22. Wei, Y., Xu, M., Liu, X., Lin, S., Pei, W., Zhou, P., Liu, H., Wu, P., Yu, Y., and Cao, C. (2020). Single-cell transcriptome analysis of the mouse and primate ovaries reveals oocyte-specific expression patterns of risk genes in ovarian aging. MedComm (2020) *4*, e209. 10.1002/mco2.209.

23. Mantri, M., Zhang, H.H., Spanos, E., Ren, Y.A., and De Vlaminck, I. (2024). A spatiotemporal molecular atlas of the ovulating mouse ovary. Proc. Natl. Acad. Sci. U S A *121*, e2317418121. 10.1073/pnas.2317418121.

24. Zhang, J., Goods, B.A., Pattarawat, P., Wang, Y., Haining, T., Zhang, Q., Shalek, A.K., Duncan, F.E., Woodruff, T.K., and Xiao, S. (2023). An ex vivo ovulation system enables the discovery of novel ovulatory pathways and nonhormonal contraceptive candidates. Biol. Reprod. *108*, 629-644. 10.1093/biolre/ioad009.

25. Hao, Y., Stuart, T., Kowalski, M.H., Choudhary, S., Hoffman, P., Hartman, A., Srivastava, A., Molla, G., Madad, S., Fernandez-Granda, C., et al. (2024). Dictionary learning for integrative, multimodal and scalable single-cell analysis. Nat. Biotechnol. *42*, 293-304. 10.1038/s41587-023-01767-y.

26. Biancalani, T., Scalia, G., Buffoni, L., Avasthi, R., Lu, Z., Sanger, A., Tokcan, N., Vanderburg, C.R., Segerstolpe, Å., Zhang, M., et al. (2021). Deep learning and alignment of spatially resolved single-cell transcriptomes with Tangram. Nat. Methods *18,* 1352-1362. 10.1038/s41592-021-01264-7.

27. Iozzo, R.V. and Schaefer, L. (2010). Proteoglycans in health and disease: novel regulatory signaling mechanisms evoked by the small leucine-rich proteoglycans. FEBS J., *277*, 3864–3875. 10.1111/j.1742-4658.2010.07797.x.

28. Wagner, M., Yoshihara, M., Douagi, I., Damdimopoulos, A., Panula, S., Petropoulos, S., Lu, H., Pettersson, K., Palm, K., Katayama, S., et al. (2020). Single-cell analysis of human ovarian cortex identifies distinct cell populations but no oogonial stem cells. Nat. Commun. *11,* 1147. 10.1038/s41467-020-14936-3.

29. Jones, A.S.K., Hannum, D.F., Machlin, J.H., Tan, A., Ma, Q., Ulrich, N.D., Shen, Y.C., Ciarelli, M., Padmanabhan, V., et al. (2024). Cellular atlas of the human ovary using morphologically guided spatial transcriptomics and single-cell sequencing. Sci. Adv. *10,* eadm7506. 10.1126/sciadv.adm7506.

30. Sato, S., Omori, Y., Katoh, K., Kondo, M., Kanagawa, M., Miyata, K., Funabiki, K., Koyasu, T., Kajimura, N., Miyoshi, T., et al. (2008). Pikachurin, a dystroglycan ligand, is essential for photoreceptor ribbon

synapse formation. Nat. Neurosci. *11*, 923-931. 10.1038/nn.2160.

31. Kanagawa, M., Omori, Y., Sato, S., Kobayashi, K., Miyagoe-Suzuki, Y., Takeda, S., Endo, T., Furukawa, T., and Toda, T. (2010). Post-translational maturation of dystroglycan is necessary for pikachurin binding and ribbon synaptic localization. J. Biol. Chem. *285*, 31208-31216. 10.1074/jbc.M110.116343.

32. Sewduth, R.N., Jaspard-Vinassa, B., Peghaire, C., Guillabert, A., Franzl, N., Larrieu-Lahargue, F., Moreau, C., Fruttiger, M., Dufourcq, P., Couffinhal, T., and Duplàa, C. (2014). The ubiquitin ligase PDZRN3 is required for vascular morphogenesis through Wnt/planar cell polarity signalling. Nat. Commun. *5*, 4832. doi: 10.1038/ncomms5832.

33. Konopelski Snavely, S.E., Susman, M.W., Kunz, R.C., Tan, J., Srinivasan, S., Cohen, M.D., Okada, K., Lamb, H., Choi, S.S., Karuna, E.P., et al. (2021). Proteomic analysis identifies the E3 ubiquitin ligase Pdzrn3 as a regulatory target of Wnt5a-Ror signaling. Proc. Natl. Acad. Sci. U S A. *118,* e2104944118. 10.1073/pnas.2104944118.

34. DeVore, N.M., and Scott, E.E. (2012). Structures of cytochrome P450 17A1 with prostate cancer drugs abiraterone and TOK-001. Nature *482,* 116–119. 10.1038/nature10743.

35. Nakajin, S., Hall, P.F., and Onoda, M. (1981). Testicular microsomal cytochrome P-450 for C21 steroid side chain cleavage. Spectral and binding studies. J. Biol. Chem. *256*, 6134–6139. 10.1016/S0021-9258(19)69138-6.

36. Chung, B.C., Picado-Leonard, J., Haniu, M., Bienkowski, M., Hall, P.F., Shively, J.E., and Miller, W.L. (1987). Cytochrome P450c17 (steroid 17 alpha-hydroxylase/17,20 lyase): Cloning of human adrenal and testis cDNAs indicates the same gene is expressed in both tissues. Proc. Natl. Acad. Sci. USA. *84*, 407–411. 10.1073/pnas.84.2.407.

37. Berkholtz, C.B., Lai, B.E., Woodruff, T.K., and Shea, L.D. (2006). Distribution of extracellular matrix proteins type I collagen, type IV collagen, fibronectin, and laminin in mouse folliculogenesis. Histochem. Cell Biol. *126*, 583-592. 10.1007/s00418-006-0194-1.

38. Richards, J.S., Ren, Y.A., Candelaria, N., Adams, J.E., and Rajkovic, A. (2018). Ovarian Follicular Theca Cell Recruitment, Differentiation, and Impact on Fertility: 2017 Update. Endocr. Rev. *39*, 1-20. 10.1210/er.2017-00164. Erratum in: Endocr. Rev. (2018) 39, 387.

39. Ancans, J., Tobin, D.J., Hoogduijn, M.J., Smit, N.P., Wakamatsu, K., and Thody, A.J. (2001). Melanosomal pH controls rate of melanogenesis, eumelanin/phaeomelanin ratio and melanosome maturation in melanocytes and melanoma cells. Exp. Cell Res. *268*, 26-35. 10.1006/excr.2001.5251.

40. Di Gioia, S.A., Letteboer, S.J., Kostic, C., Bandah-Rozenfeld, D., Hetterschijt, L., Sharon, D., Arsenijevic, Y., Roepman, R., and Rivolta, C. (2012). FAM161A, associated with retinitis pigmentosa, is a component of the cilia-basal body complex and interacts with proteins involved in ciliopathies. Hum. Mol. Genet. 21, 5174-5184. 10.1093/hmg/dds368.

41. Beryozkin, A., Matsevich, C., Obolensky, A., Kostic, C., Arsenijevic, Y., Wolfrum, U., Banin, E., and Sharon, D. (2021). A new mouse model for retinal degeneration due to Fam161a deficiency. Sci Rep. *11*, 2030. 10.1038/s41598-021-81414-1.

42. Zach, F., Grassmann, F., Langmann, T., Sorusch, N., Wolfrum, U., and Stöhr, H. (2012). The retinitis pigmentosa 28 protein FAM161A is a novel ciliary protein involved in intermolecular protein interaction and microtubule association. Hum. Mol. Genet. *21*, 4573-4586. 10.1093/hmg/dds268.

43. Lussier, J.G., Diouf, M.N., Lévesque, V., Sirois, J., and Ndiaye, K. (2017). Gene expression profiling of upregulated mRNAs in granulosa cells of bovine ovulatory follicles following stimulation with hCG. Reprod. Biol. Endocrinol. *5*, 88. 10.1186/s12958-017-0306-x.

44. Sayasith, K., Lussier, J., and Sirois, J. (2013). Molecular characterization and transcriptional regulation of a disintegrin and metalloproteinase with thrombospondin motif 1 (ADAMTS1) in bovine preovulatory follicles. Endocrinology *154*, 2857–2869. 10.1210/en.2013-1140.

45. Wang, S.J., Liu, W.J., Wu, C.J., Ma, F.H., Ahmad, S., Liu, B.R., Han, L., Jiang, X.P., Zhang, S.J., and Yang, L.G. (2012). Melatonin suppresses apoptosis and stimulates progesterone production by bovine granulosa cells via its receptors (MT1 and MT2). Theriogenology *78*, 1517–1526. 10.1016/j.theriogenology.2012.06.019.

46. He, W., Gauri, M., Li, T., Wang, R., and Lin, S.X. (2016). Current knowledge of the multifunctional 17β-hydroxysteroid dehydrogenase type 1 (HSD17B1). Gene *588*, 54–61. 10.1016/j.gene.2016.04.031.

47. Wang, S., Liu, W., Pang, X., Dai, S., and Liu, G. (2018). The Mechanism of Melatonin and Its Receptor MT2 Involved in the Development of Bovine Granulosa Cells. Int. J. Mol. Sci. *19*, 2028. 10.3390/ijms19072028.

48. Hatzirodos, N., Irving-Rodgers, H.F., Hummitzsch, K., and Rodgers, R.J. (2014). Transcriptome profiling of the theca interna from bovine ovarian follicles during atresia. PLoS One *9*, e99706. 10.1371/journal.pone.0099706.

49. Park, M., Choi, Y., Choi, H., and Roh, J. (2014). Wilms' tumor suppressor gene (WT1) suppresses apoptosis by transcriptionally downregulating BAX expression in immature rat granulosa cells. J. Ovarian Res. *7*, 118. 10.1186/s13048-014-0118-y.

50. Hanaue, M., Miwa, N., and Takamatsu, K. (2012). Immunohistochemical Characterization of S100A6 in the Murine Ovary. Acta Histochem. Cytochem. *45*, 9–14. 10.1267/ahc.11035.

51. Alfieri, C., Chang, L., Zhang, Z., Yang, J., Maslen, S., Skehel, M., and Barford, D. (2016). Molecular basis of APC/C regulation by the spindle assembly checkpoint. Nature *536*, 431–436. 10.1038/nature19083.

52. Wigglesworth, K., Lee, K.B., Emori, C., Sugiura, K., and Eppig, J.J. (2015). Transcriptomic diversification of developing cumulus and mural granulosa cells in mouse ovarian follicles. Biol. Reprod. *92*, 23.

10.1095/biolreprod.114.121756.

53. Landry, D.A., Rossi-Perazza, L., Lafontaine, S., and Sirard, M.A. (2018). Expression of atresia biomarkers in granulosa cells after ovarian stimulation in heifers. Reproduction *156*, 239–248. 10.1530/REP-18-0186.

54. Lee-Thacker, S., Choi, Y., Taniuchi, I., Takarada, T., Yoneda, Y., Ko, C., and Jo, M. (2018). Core Binding Factor β Expression in Ovarian Granulosa Cells Is Essential for Female Fertility. Endocrinology *159*, 2094-2109. 10.1210/en.2018-00011.

55. Lee-Thacker, S., Jeon, H., Choi, Y., Taniuchi, I., Takarada, T,. Yoneda, Y., Ko, C., and Jo, M. (2020). Core Binding Factors are essential for ovulation, luteinization, and female fertility in mice. Sci. Rep. *10*, 9921. 10.1038/s41598-020-64257-0.

56. Dinh, D.T., Breen, J., Nicol, B., Foot, N.J., Bersten, D.C., Emery, A., Smith, K.M., Wong, Y.Y., Barry, S.C., Yao, H.H.C., et al. (2023). Progesterone receptor mediates ovulatory transcription through RUNX transcription factor interactions and chromatin remodelling. Nucleic Acids Res. *51*, 5981-5996. 10.1093/nar/gkad271.

57. Breiden, B. and Sandhoff, K. (2019). Lysosomal Glycosphingolipid Storage Diseases. Annu. Rev. Biochem. *88*, 461-485. 10.1146/annurev-biochem-013118-111518.

58. Choo, Y.K., Chiba, K., Tai, T., Ogiso, M., and Hoshi, M. (1995). Differential distribution of gangliosides in adult rat ovary during the oestrous cycle. Glycobiology. *5*, 299-309. 10.1093/glycob/5.3.299.

59. Choo, Y.K. (1999). Distribution of ganglioside GM3 in the rat ovary after gonadotropin stimulation. Mol. Cells. *9*, 365-375.

60. Kishimoto, K., Nishizuka, M., Katoh, D., Kato, A., Osada, S., and Imagawa, M. (2013). FAD104, a regulatory factor of adipogenesis, acts as a novel regulator of calvarial bone formation. J. Biol. Chem. *288*, 31772–31783. 10.1074/jbc.M113.452961.

61. Cai, C., Rajaram, M., Zhou, X., Liu, Q., Marchica, J., Li, J., and Powers, R. S. (2012). Activation of multiple cancer pathways and tumor maintenance function of the 3q amplified oncogene FNDC3B. Cell Cycle *11*, 1773–1781. 10.4161/cc.20121.

62. Wuensch, T., Wizenty, J., Quint, J., Spitz, W., Bosma, M., Becker, O., Adler, A., Veltzke-Schlieker, W., Stockmann, M., Weiss, S., et al. (2019). Expression Analysis of Fibronectin Type III Domain-Containing (FNDC) Genes in Inflammatory Bowel Disease and Colorectal Cancer. Gastroenterol. Res. Pract. 2019, 3784172. 10.1155/2019/3784172.

63. Poretsky, L., Islam, J., Avtanski, D., Lin, Y. K., Shen, Y. L., Hirth, Y., Lesser, M., Rosenwaks, Z., and Seto-Young, D. (2017). Reproductive effects of irisin: Initial in vitro studies. Reprod. Biol. *17*, 285–288. 10.1016/j.repbio.2017.05.011.

64. Basini, G., Bussolati, S., Iannarelli, M., Ragionieri, L., Grolli, S., Ramoni, R., Dodi, A., Gazza, F., and Grasselli, F. (2021). The myokine irisin: localization and effects in swine late medium and large antral ovarian follicle. Domest. Anim. Endocrinol. *74*, 106576. 10.1016/j.domaniend.2020.106576.

65. Luo, Y., Qiao, X., Ma, Y., Deng, H., Xu, C.C., and Xu, L. (2021). Irisin deletion induces a decrease in growth and fertility in mice. Reprod. Biol. Endocrinol. *19*, 22. 10.1186/s12958-021-00702-7.

66. Mara, J.N., Zhou, L.T., Larmore, M., Johnson, B., Ayiku, R., Amargant, F., Pritchard, M.T., and Duncan, F.E. (2020). Ovulation and ovarian wound healing are impaired with advanced reproductive age. Aging *12*, 9686–9713. 10.18632/aging.103237

67. Nio-Kobayashi, J. and Iwanaga, T. (2010). Differential cellular localization of galectin-1 and galectin-3 in the regressing corpus luteum of mice and their possible contribution to luteal cell elimination. J. Histochem. Cytochem. *58*, 741–749. 10.1369/jhc.2010.956227.

68. Song, W.C. (2001). Biochemistry and reproductive endocrinology of estrogen sulfotransferase. Ann. N. Y. Acad. Sci. *948*, 43–50.

69. Cole, G.B., Keum, G., Liu, J., Small, G.W., Satyamurthy, N., Kepe, V., and Barrio, J.R. (2010). Specific estrogen sulfotransferase (SULT1E1) substrates and molecular imaging probe candidates. Proc. Natl. Acad. Sci. U S A. *107*, 6222–6227.

70. Falany, C.N. (1997). Enzymology of human cytosolic sulfotransferases. FASEB J. *11*, 206–216.

71. Krawetz, S. A. (1994). The origin of lysyl oxidase. Comparative Biochemistry and Physiology Part B: Comparative Biochemistry *108*, 117-119.

72. Slee, R.B., Hillier, S.G., Largue, P., Harlow, C.R., Miele, G., and Clinton, M. (2001). Differentiation-dependent expression of connective tissue growth factor and lysyl oxidase messenger ribonucleic acids in rat granulosa cells. Endocrinology *142*, 1082-1089.

73. Kendall, N.R., Marsters, P., Scaramuzzi, R.J., and Campbell, B.K. (2003). Expression of lysyl oxidase and effect of copper chloride and ammonium tetrathiomolybdate on bovine ovarian follicle granulosa cells cultured in serum-free media. Reproduction *125*, 657-665.

74. Hernandez-Gonzalez, I., Gonzalez-Robayna, I., Shimada, M., Wayne, C.M., Ochsner, S.A., White, L., and Richards, J.S. (2006). Gene expression profiles of cumulus cell oocyte complexes during ovulation reveal cumulus cells express neuronal and immune-related genes: does this expand their role in the ovulation process? Mol. Endocrinol. *20*, 1300-1321. 10.1210/me.2005-0420.

75. Salustri, A., Yanagishita, M., and Hascall, V.C. (1989). Synthesis and accumulation of hyaluronic acid and proteoglycans in the mouse cumulus cell-oocyte complex during follicle-stimulating hormone-induced mucification. J. Biol. Chem. *264*, 13840–13847.

76. Chen, L., Wert, S.E., Hendrix, E.M., Russell, P.T., Cannon, M., and Larsen, W.J. (1990). Hyaluronic acid synthesis and gap junction endocytosis are necessary for normal expansion of the cumulus mass. Mol. Reprod. Dev. *26*, 236–247. 10.1002/mrd.1080260307.

77. Fülöp, C., Salustri, A., and Hascall, V.C. (1997). Coding sequence of a hyaluronan synthase homologue expressed during expansion of the mouse cumulus-oocyte complex. Arch. Biochem. Biophys. *337*, 261–266. 10.1006/abbi.1996.9793.

78. Carrette, O., Nemade, R.V., Day, A.J., Brickner, A., and Larsen, W.J. (2001). TSG-6 is concentrated in the extracellular matrix of mouse cumulus oocyte complexes through hyaluronan and inter-alpha-inhibitor binding. Biol. Reprod. *65*, 301–308. 10.1095/biolreprod65.1.301.

79. Rodgers, R.J. and Irving-Rodgers, H.F. (2010). Formation of the ovarian follicular antrum and follicular fluid. Biol. Reprod. *82*, 1021–1029. 10.1095/biolreprod.109.082941.

80. Clarke, H.G., Hope, S.A., Byers, S., and Rodgers, R.J. (2006). Formation of ovarian follicular fluid may be due to the osmotic potential of large glycosaminoglycans and proteoglycans. Reproduction *132*, 119–131. 10.1530/rep.1.00960.

81. Biase, F.H. and Kimble, K.M.. (2018). Functional signaling and gene regulatory networks between the oocyte and the surrounding cumulus cells. BMC Genomics *19*, 351. 10.1186/s12864-018-4738-2.

82. Hizaki, H., Segi, E., Sugimoto, Y., Hirose, M., Saji, T., Ushikubi, F., Matsuoka, T., Noda, Y., Tanaka, T., Yoshida, N., et al. (1999). Abortive expansion of the cumulus and impaired fertility in mice lacking the prostaglandin E receptor subtype EP(2). Proc. Natl. Acad. Sci. U S A *96*, 10501–10506. 10.1073/pnas.96.18.10501.

83. Liu, Z., Fan, H.Y., Wang, Y., and Richards, J.S. (2010). Targeted disruption of Mapk14 (p38MAPKalpha) in granulosa cells and cumulus cells causes cell-specific changes in gene expression profiles that rescue COC expansion and maintain fertility. Mol. Endocrinol. *24*, 1794–1804. 10.1210/me.2010-0086.

84. Ben-Ami, I., Freimann, S., Armon, L., Dantes, A., Strassburger, D., Friedler, S., Raziel, A., Seger, R., Ron-El, R., and Amsterdam, A. (2006). PGE2 up-regulates EGF-like growth factor biosynthesis in human granulosa cells: new insights into the coordination between PGE2 and LH in ovulation. Mol. Hum. Reprod. *12*, 593–599. 10.1093/molehr/gal068.

85. Blaha, M., Prochazka, R., Adamkova, K., Nevoral, J., and Nemcova, L. (2017). Prostaglandin E2 stimulates the expression of cumulus expansion-related genes in pigs: the role of protein kinase B. Prostaglandins Other Lipid Mediat. *130*, 38–46. 10.1016/j.prostaglandins.2017.04.001.

86. Yodoi, R., Tamba, S., Morimoto, K., Segi-Nishida, E., Nishihara, M., Ichikawa, A., Narumiya, S., and Sugimoto, Y. (2009). RhoA/Rho kinase signaling in the cumulus mediates extracellular matrix assembly. Endocrinology *150*, 3345–3352. 10.1210/en.2008-1449.

87. McNatty, K.P., Smith, D.M., Makris, A., Osathanondh, R., & Ryan, K.J. (1980). Steroidogenesis by the human oocyte-cumulus cell complex in vitro. Steroids *35*, 643–651. 10.1016/0039-128x(80)90089-6.

88. Vanderhyden, B.C., and Tonary, A.M. (1995). Differential regulation of progesterone and estradiol production by mouse cumulus and mural granulosa cells by A factor(s) secreted by the oocyte. Biol. Reprod. *53*, 1243–1250. 10.1095/biolreprod53.6.1243.

89. Vanderhyden, B.C., Cohen, J.N., and Morley, P. (1993). Mouse oocytes regulate granulosa cell steroidogenesis. Endocrinology *133*, 423–426. 10.1210/endo.133.1.8319589.

90. Sherizly, I., and Kraicer, P.F. (1980). Progesterone secretion by the post□ovulatory rat cumulus oophorus. Gamete Research *3*, 115-119. https://doi.org/10.1002/mrd.1120030203.

91. Channing, C.P., Bae, I.H., Stone, S.L., Anderson, L.D., Edelson, S., and Fowler, S.C. (1981). Porcine granulosa and cumulus cell properties LH/hCG receptors, ability to secrete progesterone and ability to respond to LH. Mol. Cell. Endocrinol. *22*, 359-370. 10.1016/0303-7207(81)90044-7.

92. Mingoti, G.Z., Garcia, J.M., and Rosa-e-Silva, A.A. (2002). Steroidogenesis in cumulus cells of bovine cumulus-oocyte-complexes matured in vitro with BSA and different concentrations of steroids. Anim. Reprod. Sci. *69*, 175–186. 10.1016/s0378-4320(01)00187-7.

93. Wang, H.F., Isobe, N., Kumamoto, K., Yamashiro, H., Yamashita, Y., and Terada, T. (2006). Studies of the role of steroid hormone in the regulation of oocyte maturation in cattle. Reprod. Biol. Endocrinol. *4*, 4. 10.1186/1477-7827-4-4.

94. Yamashita, Y., Shimada, M., Okazaki, T., Maeda, T., and Terada, T. (2003). Production of progesterone from de novo-synthesized cholesterol in cumulus cells and its physiological role during meiotic resumption of porcine oocytes. Biol. Reprod. *68*, 1193–1198. 10.1095/biolreprod.102.010934.

95. Shimada, M., and Terada, T. (2002). FSH and LH induce progesterone production and progesterone receptor synthesis in cumulus cells: a requirement for meiotic resumption in porcine oocytes. Mol. Hum. Reprod. *8*, 612–618. 10.1093/molehr/8.7.612.

96. Shimada, M., Umehara, T., and Hoshino, Y. (2016). Roles of epidermal growth factor (EGF)-like factor in the ovulation process. Reprod. Med. Biol. *15*, 201–216. 10.1007/s12522-016-0236-x.

97. Yamashita, Y. and Shimada, M. (2012). The release of EGF domain from EGF-like factors by a specific cleavage enzyme activates the EGFR-MAPK3/1 pathway in both granulosa cells and cumulus cells during the ovulation process. J. Reprod. Dev. *58*, 510–514. 10.1262/jrd.2012-056.

98. Kõks, S., Velthut, A., Sarapik, A., Altmäe, S., Reinmaa, E., Schalkwyk, L.C., Fernandes, C., Lad, H.V., Soomets, U., Jaakma, U., *et al.* (2010). The differential transcriptome and ontology profiles of floating and cumulus granulosa cells in stimulated human antral follicles. Mol. Hum. Reprod. *16*, 229–240. 10.1093/molehr/gap103.

99. Sasseville, M., Gagnon, M.C., Guillemette, C., Sullivan, R., Gilchrist, R.B., and Richard, F.J. (2009). Regulation of gap junctions in porcine cumulus-oocyte complexes: contributions of granulosa cell contact, gonadotropins, and lipid rafts. Mol. Endocrinol. *23*, 700–710. 10.1210/me.2008-0320.

100. Shirafuta, Y., Tamura, I., Shiroshita, A., Fujimura, T., Maekawa, R., Taketani, T., and Sugino, N. (2024). Analysis of cell-cell interaction between mural granulosa cells and cumulus granulosa cells during ovulation using single-cell RNA sequencing data of mouse ovary. Reprod. Med. Biol. *23*, e12564. 10.1002/rmb2.12564.

101. Berkholtz, C.B., Shea, L.D., and Woodruff, T.K. (2006). Extracellular matrix functions in follicle maturation. Semin. Reprod. Med. *24*, 262-269. 10.1055/s-2006-948555.

102. Irving-Rodgers, H.F., Hummitzsch, K., Murdiyarso, L.S., Bonner, W.M., Sado, Y., Ninomiya, Y., Couchman, J.R., Sorokin, L.M., and Rodgers, R.J. (2010). Dynamics of extracellular matrix in ovarian follicles and corpora lutea of mice. Cell Tissue Res. *339*, 613-624. 10.1007/s00441-009-0905-8.

103. Monniaux, D., Huet-Calderwood, C., Le Bellego, F., Fabre, S., Monget, P., and Calderwood, D.A. (2006). Integrins in the ovary. Semin. Reprod. Med. *24*, 251-261. 10.1055/s-2006-948554.

104. Erickson, G.F. and Shimasaki, S. (2003). The spatiotemporal expression pattern of the bone morphogenetic protein family in rat ovary cell types during the estrous cycle. Reprod. Biol. Endocrinol. *1,* 9. 10.1186/1477-7827-1-9.

105. Yi, S.E., LaPolt, P.S., Yoon, B.S., Chen, J.Y., Lu, J.K., and Lyons, K.M. (2001). The type I BMP receptor BmprIB is essential for female reproductive function. Proc. Natl. Acad. Sci. U S A. *98*, 7994-7999. 10.1073/pnas.141002798.

106. Edson, M.A., Nalam, R.L., Clementi, C., Franco, H.L., Demayo, F.J., Lyons, K.M., Pangas, S.A., and Matzuk, M.M. (2010). Granulosa cell-expressed BMPR1A and BMPR1B have unique functions in regulating fertility but act redundantly to suppress ovarian tumor development. Mol Endocrinol. *24*, 1251-1266. 10.1210/me.2009-0461.

107. Nio-Kobayashi, J., Trendell, J., Giakoumelou, S., Boswell, L., Nicol, L., Kudo, M., Sakuragi, N., Iwanaga, T., and Duncan, W.C. (2015). Bone morphogenetic proteins are mediators of luteolysis in the human corpus luteum. Endocrinology. *156*, 1494-1503. 10.1210/en.2014-1704.

108. Monaco, C.F., Plewes, M.R., Przygrodzka, E., George, J.W., Qiu, F., Xiao, P., Wood, J.R., Cupp, A.S., and Davis, J.S. (2023). Basic fibroblast growth factor induces proliferation and collagen production by fibroblasts derived from the bovine corpus luteum. Biol. Reprod. *109*, 367-380. 10.1093/biolre/ioad065.

109. Ishiguro, K., Kojima, T., Taguchi, O., Saito, H., Muramatsu, T., and Kadomatsu, K. (1999). Syndecan-4 expression is associated with follicular atresia in mouse ovary. Histochem. Cell. Biol. *112*, 25-33. 10.1007/s004180050388.

110. Gospodarowicz, D., Massoglia, S., Cheng, J., and Fujii, D.K. (1986) Effect of fibroblast growth factor and lipoproteins on the proliferation of endothelial cells derived from bovine adrenal cortex, brain cortex, and corpus luteum capillaries. J. Cell. Physiol. *127*, 121–136. 10.1002/jcp.1041270116.

111. Robinson, R.S., Nicklin, L.T., Hammond, A.J., Schams, D., Hunter, M.G., and Mann, G.E. (2007). Fibroblast growth factor 2 is more dynamic than vascular endothelial growth factor A during the follicle–luteal transition in the cow. Biol. Reprod. *77*, 28–36. 10.1095/biolreprod.106.055434.

112. Bellin, R., Capila, I., Lincecum, J., Park, P.W., Reizes, O., and Bernfield, M.R. (2002). Unlocking the secrets of syndecans: Transgenic organisms as a potential key. Glycoconj. J. *19, 295–304.* 10.1023/a:1025352501148.

113. Couchman, J.R. (2003). Syndecans: proteoglycan regulators of cell-surface microdomains? Nat. Rev. Mol. Cell. Biol. *4*, 926-937. 10.1038/nrm1257.

114. Watson, L.N., Mottershead, D.G., Dunning, K.R., Robker, R.L., Gilchrist, R.B., and Russell, D.L. (2012). Heparan sulfate proteoglycans regulate responses to oocyte paracrine signals in ovarian follicle morphogenesis. Endocrinology *153*, 4544-4555. 10.1210/en.2012-1181.

115. Reich, R., Daphna-Iken, D., Chun, S.Y., Popliker, M., Slager, R., Adelmann-Grill, B.C., and Tsafriri, A. (1991). Preovulatory changes in ovarian expression of collagenases and tissue metalloproteinase inhibitor messenger ribonucleic acid: role of eicosanoids. Endocrinology *129*, 1869–1875. 10.1210/endo-129-4-1869.

116. Mann, J.S., Kindy, M.S., Edwards, D.R., and Curry, T.E. (1991). Hormonal regulation of matrix metalloproteinase inhibitors in rat granulosa cells and ovaries. Endocrinology *128*, 1825–1832. 10.1210/endo-128-4-1825.

117. Curry, T.E. and Osteen, K.G. (2001). Cyclic changes in the matrix metalloproteinase system in the ovary and uterus. Biol. Reprod. *64*, 1285–1296. 10.1095/biolreprod64.5.1285.

118. Curry, T.E., Osteen, K.G. (2003). The matrix metalloproteinase system: changes, regulation, and impact throughout the ovarian and uterine reproductive cycle. Endocr. Rev. *24*, 428–465. 10.1210/er.2002-0005.

119. Wassarman, P.M. and Josefowicz, W.J. (1978). Oocyte development in the mouse: an ultrastructural comparison of oocytes isolated at various stages of growth and meiotic competence. J Morphol. *156,* 209–235. 10.1002/jmor.1051560206

120. Chen, S. and Birk, D.E. (2013). The regulatory roles of small leucine-rich proteoglycans in extracellular matrix assembly. FEBS J. *280*, 2120-2137. 10.1111/febs.12136.

121. Park, B.S., Lee, J., and Jun, J.H. (2021). Decorin: a multifunctional proteoglycan involved in oocyte maturation and trophoblast migration. Clin. Exp. Reprod. Med. *48*, 303-310. 10.5653/cerm.2021.05071.

122. Park, J.Y., Su, Y.Q., Ariga, M., Law, E., Jin, S.L., and Conti, M. (2004). EGF-like growth factors as mediators of LH action in the ovulatory follicle. Science *303*, 682-684. 10.1126/science.1092463.

123. Panigone, S., Hsieh, M., Fu, M., Persani, L., and Conti, M. (2008). Luteinizing hormone signaling in preovulatory follicles involves early activation of the epidermal growth factor receptor pathway. Mol. Endocrinol. *22*, 924-936. 10.1210/me.2007-0246.

124. Kenngott, R.A., Scholz, W., and Sinowatz, F. (2016). Ultrastructural Aspects of the Prenatal Bovine Ovary Differentiation with a Special Focus on the Interstitial Cells. Anat. Histol. Embryol. *45*, 357–366. 10.1111/ahe.12203.

125. Abd-Elkareem, M. (2017). Cell-specific immuno-localization of progesterone receptor alpha in the rabbit ovary during pregnancy and after parturition. Anim. Reprod. Sci. *180*, 100–120. 10.1016/j.anireprosci.2017.03.007.

126. Konishi, I., Fujii, S., Okamura, H., Parmley, T., and Mori, T. (1986). Development of interstitial cells and ovigerous cords in the human fetal ovary: an ultrastructural study. J. Anat. *148*, 121–135.

127. Candelaria, N.R., Padmanabhan, A., Stossi, F., Ljungberg, M.C., Shelly, K.E., Pew, B.K., Solis, M., Rossano, A.M., McAllister, J.M., Wu, S., *et al.* (2019). VCAM1 Is Induced in Ovarian Theca and Stromal Cells in a Mouse Model of Androgen Excess. Endocrinology *160*, 1377–1393. 10.1210/en.2018-00731.

128. Wagner, M., Yoshihara, M., Douagi, I., Damdimopoulos, A., Panula, S., Petropoulos, S., Lu, H., Pettersson, K., Palm, K., Katayama, S., *et al.* (2020). Single-cell analysis of human ovarian cortex identifies distinct cell populations but no oogonial stem cells. Nat. Commun. *11*, 1147. 10.1038/s41467-020-14936-3.

129. Wang, S., Zheng, Y., Li, J., Yu, Y., Zhang, W., Song, M., Liu, Z., Min, Z., Hu, H., Jing, Y., et al. (2020). Single-Cell Transcriptomic Atlas of Primate Ovarian Aging. Cell *180*, 585–600.e19. 10.1016/j.cell.2020.01.009.

130. Hillier, S. G., Whitelaw, P. F., and Smyth, C.D. (1994). Follicular oestrogen synthesis: the 'two-cell, two-gonadotrophin'model revisited. Mol. Cell. Endocrinol. *100*, 51-54. 10.1016/0303-7207(94)90278-x.

131. Atkinson, A. and Winge, D.R. (2009). Metal acquisition and availability in the mitochondria. Chem. Rev. *109*, 4708–4721. 10.1021/cr900006y.

132. Stouffer, R.L. and Hennebold, J.D. (2015). Structure, function, and regulation of the corpus luteum. In eds. Knobil and Neill's Physiology of Reproduction, Plant T.M. and Zeleznik A.J., eds. (Academic Press), pp.1023–1076.

133. Stocco, C., Telleria, C., and Gibori, G. (2007). The molecular control of corpus luteum formation, function, and regression. Endocr. Rev. *28*, 117-49. 10.1210/er.2006-0022.

134. Akison, L.K., Alvino, E.R., Dunning, K.R., Robker, R.L., and Russell, D.L. (2012). Transient invasive migration in mouse cumulus oocyte complexes induced at ovulation by luteinizing hormone. Biol. Reprod. *86*, 125. 10.1095/biolreprod.111.097345.

135. Motta, P.M., Nottola, S.A., Familiari, G., Machiarelli, G., Correr, S., and Makabe, S. (1999). Structure and function of the human oocyte-cumulus-corona cell complex before and after ovulation. *Protoplasma 206*, 270–277. 10.1007/BF01288215.

136. Abbassi, L., El-Hayek, S., Carvalho, K.F., Wang, W., Yang, Q., Granados-Aparici, S., Mondadori, R., Bordignon, V., and Clarke, H.J. (2021). Epidermal growth factor receptor signaling uncouples germ cells from the somatic follicular compartment at ovulation. Nat. Commun. *12*, 1438. 10.1038/s41467-021-21644-z.

137. Clarke, H.J. (2022). Transzonal projections: Essential structures mediating intercellular communication in the mammalian ovarian follicle. Mol. Reprod. Dev. *89*, 509-525. 10.1002/mrd.23645.

138. Teves, M.E., Barbano, F., Guidobaldi, H.A., Sanchez, R., Miska, W., and Giojalas, L.C. (2006). Progesterone at the picomolar range is a chemoattractant for mammalian spermatozoa. Fert. Steril. *86*, 745–749. 10.1016/j.fertnstert.2006.02.080.

139. LeMaire, G.S. (1987). The luteinized unruptured follicle syndrome: anovulation in disguise, J. Obstet. Gynecol. Neonatal Nurs. *16*, 116-120.

140. Hamilton, C.J., Wetzels, L.C., Evers, J.L., Hoogland, H.J., Muitjens, A., and De Haan, J. (1985). Follicle growth curves and hormonal patterns in patients with the luteinized unruptured follicle syndrome. Fertil. Steril. *43*, 541-548.

141. Marik, J. and Hulka, J. (1978). Luteinized unruptured follicle syndrome: a subtle cause of infertility. Fertil. Steril. *29*, 270-274.

142. Dal, J., Vural, B., Caliskan, E., Ozkan, S., and Yucesoy, I. (2005). Power Doppler ultrasound studies of ovarian, uterine, and endometrial blood flow in regularly menstruating women with respect to luteal phase defects. Fertil Steril. 84, 224–227.

143. Qublan, H., Amarin, Z., Nawasreh, M., Diab, F., Malkawi, S., Al-Ahmad, N., and Balawneh, M. (2006). Luteinized unruptured follicle syndrome: incidence and recurrence rate in infertile women with unexplained infertility undergoing intrauterine insemination. Hum Reprod. *21*, 2110–2113.

144. McGinnis, C.S., Murrow, L.M., and Gartner, Z.J. (2019). DoubletFinder: Doublet Detection in Single-Cell RNA Sequencing Data Using Artificial Nearest Neighbors. Cell Syst. *8*, 329-337.e4. 10.1016/j.cels.2019.03.003.

145. Finak, G., McDavid, A., Yajima, M., Deng, J., Gersuk, V., Shalek, A.K., Slichter, C.K., Miller, H.W., McElrath, M.J., Prlic, M., *et al.* (2015). MAST: a flexible statistical framework for assessing transcriptional changes and characterizing heterogeneity in single-cell RNA sequencing data. Genome Biol. *16*, 278.

10.1186/s13059-015-0844-5.

146. Jin, S., Guerrero-Juarez, C.F., Zhang, L., Chang, I., Ramos, R., Kuan, C.H., Myung, P., Plikus, M.V., and Nie, Q. (2021). Inference and analysis of cell-cell communication using CellChat. Nat. Commun. *12*, 1088. 10.1038/s41467-021-21246-9.

147. Browaeys, R., Gilis, J., Sang-Aram, C., De Bleser, P., Hoste, L., Tavernier, S., Lambrechts, D., Seurinck, R., and Saeys, Y. (2023). MultiNicheNet: a flexible framework for differential cell-cell communication analysis from multi-sample multi-condition single-cell transcriptomics data. Preprint at bioRxiv, 10.1101/2023.06.13.544751.

148. Ashburner, M., Ball, C.A., Blake, J.A., Botstein, D., Butler, H., Cherry, J.M., Davis, A.P., Dolinski, K., Dwight, S.S., Eppig, J.T., *et al.* (2000). Gene ontology: tool for the unification of biology. The Gene Ontology Consortium. Nat. Genet. *25*, 25-9. 10.1038/75556.

149. Milacic, M., Beavers, D., Conley, P., Gong, C., Gillespie, M., Griss, J., Haw, R., Jassal, B., Matthews, L., May, B., et al. (2024). The Reactome Pathway Knowledgebase 2024. Nucleic Acids Res. 10.1093/nar/gkad1025.

150. Kanehisa, M., Furumichi, M., Sato, Y., Kawashima, M. and Ishiguro-Watanabe, M. (2023). KEGG for taxonomy-based analysis of pathways and genomes. Nucleic Acids Res. *51*, D587-D592.

151. Kuleshov, M. V., Jones, M. R., Rouillard, A. D., Fernandez, N. F., Duan, Q., Wang, Z., Koplev, S., Jenkins, S. L., Jagodnik, K. M., Lachmann, A., McDermott, M. G., Monteiro, C. D., Gundersen, G. W., & Ma'ayan, A. (2016). Enrichr: a comprehensive gene set enrichment analysis web server 2016 update. Nucleic Acids res, *44*, W90–W97. 10.1093/nar/gkw377

152. Emanuel, G., Eichhorn, S.W., and Zhuang, X. (2020). MERlin - scalable and extensible MERFISH analysis software, v0.1.6. Zenodo, 10.5281/zenodo.3758540.

153. Stringer, C., Wang, T., Michaelos, M., and Pachitariu, P. (2021). Cellpose: a generalist algorithm for cellular segmentation. Nat. Methods *18*, 100–106. 10.1038/s41592-020-01018-x.

154. Wolf, F.A., Angerer, P., and Theis, F.J. (2018). SCANPY: large-scale single-cell gene expression data analysis. Genome Biol. *19*, 15. 10.1186/s13059-017-1382-0.

155. Palla, G., Spitzer, H., Klein, M., Fischer, D., Schaar, A.C., Kuemmerle, L.B., Rybakov, S., Ibarra, I.L., Holmberg, O., Virshup, I., et al. (2022). *et al.* Squidpy: a scalable framework for spatial omics analysis. Nat. Methods *19*, 171-178. 10.1038/s41592-021-01358-2.

156. Efremova, M., Vento-Tormo, M., Teichmann, S.A., and Vento-Tormo, R. (2020). CellPhoneDB: inferring cell-cell communication from combined expression of multi-subunit ligand-receptor complexes. Nat. Protoc. *15*, 1484-1506. 10.1038/s41596-020-0292-x.

157. Schindelin, J., Arganda-Carreras, I., Frise, E., Kaynig, V., Longair, M., Pietzsch, T., Preibisch, S., Rueden, C., Saalfeld, S., Schmid, B., Tinevez, J. Y., White, D. J., Hartenstein, V., Eliceiri, K., Tomancak, P., & Cardona, A. (2012). Fiji: an open-source platform for biological-image analysis. Nat. Methods *9,* 676–682. 10.1038/nmeth.2019

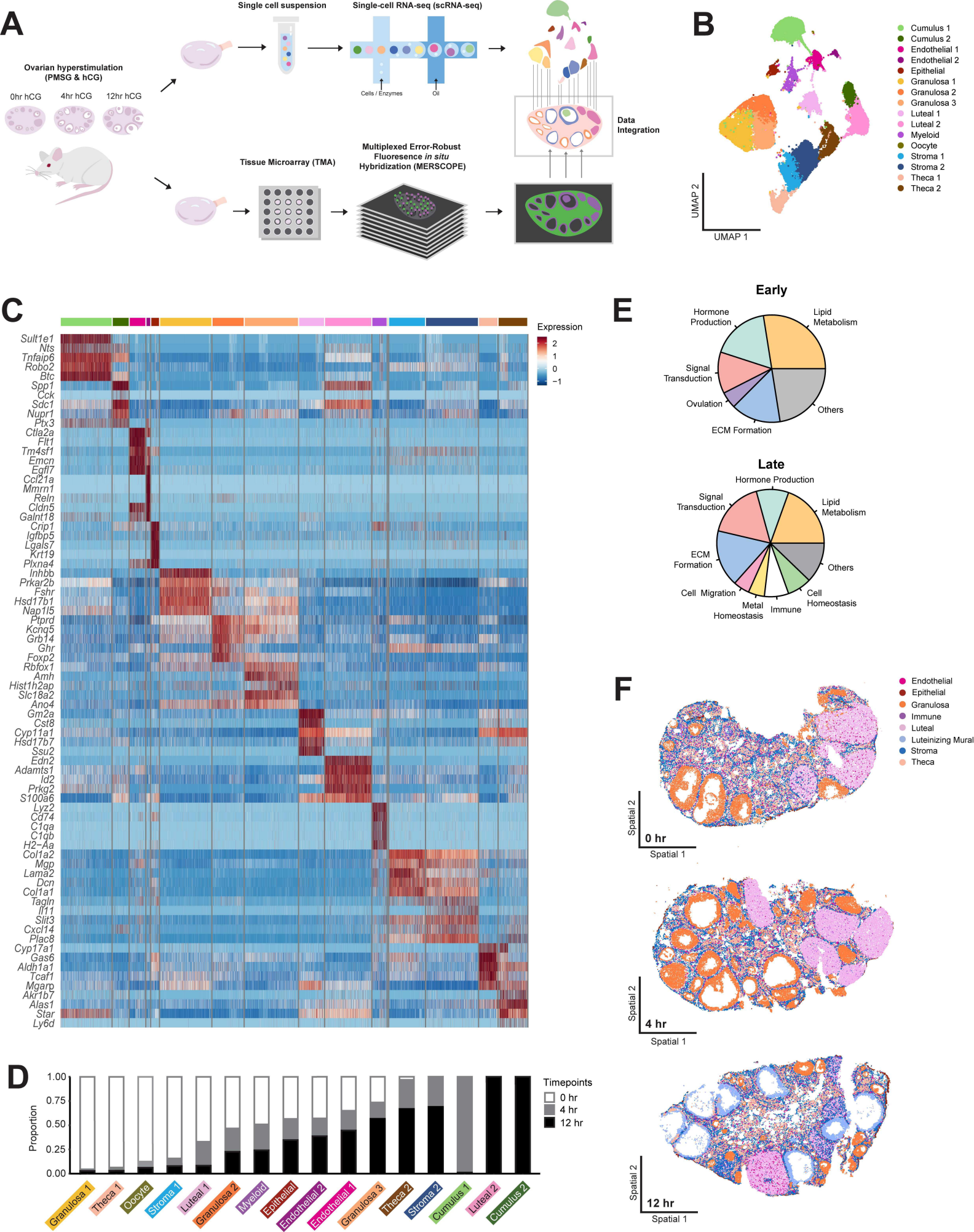
A
Ovarian hyperstimulation
(PMSG & hCG)
0hr hCG
4hr hCG
12hr hCG
Single cell suspension
Single-cell RNA-seq (scRNA-seq)
Cells / Enzymes
Oil
Data
Integration
Tissue Microarray (TMA)
Multiplexed Error-Robust
Fluoresence in situ
Hybridization (MERSCOPE)
B
Cumulus 1
Cumulus 2
Endothelial 1
Endothelial 2
Epithelial
Granulosa 1
Granulosa 2
Granulosa 3
Luteal 1
Luteal 2
Myeloid
Oocyte
Stroma 1
Stroma 2
Theca 1
Theca 2
UMAP 2
UMAP 1
C
Expression
2
1
0
−1
Sult1e1
Nts
Tnfaip6
Robo2
Btc
Spp1
Cck
Sdc1
Nupr1
Ptx3
Ctla2a
Flt1
Tm4sf1
Emcn
Egfl7
Ccl21a
Mmrn1
Reln
Cldn5
Galnt18
Crip1
Igfbp5
Lgals7
Krt19
Plxna4
Inhbb
Prkar2b
Fshr
Hsd17b1
Nap1l5
Ptprd
Kcnq5
Grb14
Ghr
Foxp2
Rbfox1
Amh
Hist1h2ap
Slc18a2
Ano4
Gm2a
Cst8
Cyp11a1
Hsd17b7
Ssu2
Edn2
Adamts1
Id2
Prkg2
S100a6
Lyz2
Cd74
C1qa
C1qb
H2−Aa
Col1a2
Mgp
Lama2
Dcn
Col1a1
Tagln
Il11
Slit3
Cxcl14
Plac8
Cyp17a1
Gas6
Aldh1a1
Tcaf1
Mgarp
Akr1b7
Alas1
Star
Ly6d
E
Early
Hormone Production
Lipid Metabolism
Signal Transduction
Ovulation
Others
ECM Formation
Late
Hormone Production
Signal Transduction
Lipid Metabolism
ECM Formation
Others
Cell Migration
Metal Homeostasis
Immune
Cell Homeostasis
F
Endothelial
Epithelial
Granulosa
Immune
Luteal
Luteinizing Mural
Stroma
Theca
Spatial 2
0 hr
Spatial 1
Spatial 2
4 hr
Spatial 1
Spatial 2
12 hr
Spatial 1
D
Proportion
1.00
0.75
0.50
0.25
0.00
Timepoints
0 hr
4 hr
12 hr
Granulosa 1
Theca 1
Oocyte
Stroma 1
Luteal 1
Granulosa 2
Myeloid
Epithelial
Endothelial 2
Endothelial 1
Granulosa 3
Theca 2
Stroma 2
Cumulus 1
Luteal 2
Cumulus 2

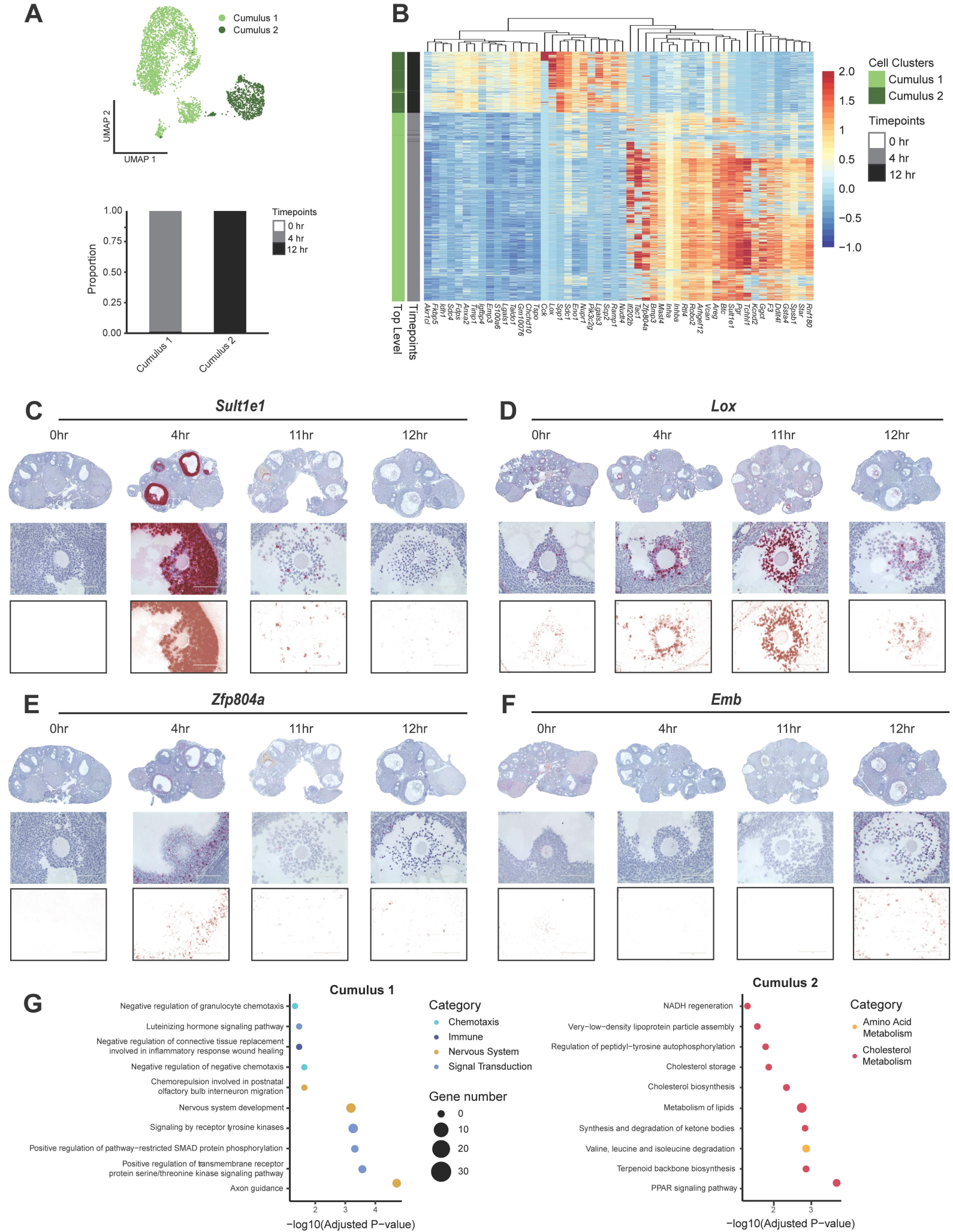
A
Cumulus 1
Cumulus 2
UMAP 2
UMAP 1
Proportion
1.00
0.75
0.50
0.25
0.00
Cumulus 1
Cumulus 2
Timepoints
0 hr
4 hr
12 hr
B
Cell Clusters
Cumulus 1
Cumulus 2
Timepoints
0 hr
4 hr
12 hr
2.0
1.5
1
0.5
0.0
−0.5
−1.0
Top Level
Timepoints
Akr1c1
Fhdpf5
Idh1
Sdc4
Fdps
Anxa2
Timp1
Igfbp4
Emp3
S100a6
Lgals1
Tald01
Gm10076
Cstb
Ctsb
Ccl
Cck
Lox
Spp1
Sdc1
Eno1
Nupr1
Pik3c2g
Lgals3
Scp2
Ramp1
Nudt4
Ifi202b
Zfp804a
Bmp3
Mast4
Inha
Inhba
Rtl4
Robo2
Arhgef12
Vcan
Areg
Btc
Sult1e1
Pgr
Tcfcp2l1
Ggct
F3
Ddit4l
Gsta4
Spsb1
Star
Rnf180
C
Sult1e1
0hr
4hr
11hr
12hr
D
Lox
0hr
4hr
11hr
12hr
E
Zfp804a
0hr
4hr
11hr
12hr
F
Emb
0hr
4hr
11hr
12hr
G
Cumulus 1
Negative regulation of granulocyte chemotaxis
Luteinizing hormone signaling pathway
Negative regulation of connective tissue replacement involved in inflammatory response wound healing
Negative regulation of negative chemotaxis
Chemorepulsion involved in postnatal olfactory bulb interneuron migration
Nervous system development
Signaling by receptor tyrosine kinases
Positive regulation of pathway−restricted SMAD protein phosphorylation
Positive regulation of transmembrane receptor protein serine/threonine kinase signaling pathway
Axon guidance
2
3
4
−log10(Adjusted P−value)
Category
Chemotaxis
Immune
Nervous System
Signal Transduction
Gene number
0
10
20
30
Cumulus 2
NADH regeneration
Very−low−density lipoprotein particle assembly
Regulation of peptidyl−tyrosine autophosphorylation
Cholesterol storage
Cholesterol biosynthesis
Metabolism of lipids
Synthesis and degradation of ketone bodies
Valine, leucine and isoleucine degradation
Terpenoid backbone biosynthesis
PPAR signaling pathway
2
3
−log10(Adjusted P−value)
Category
Amino Acid Metabolism
Cholesterol Metabolism

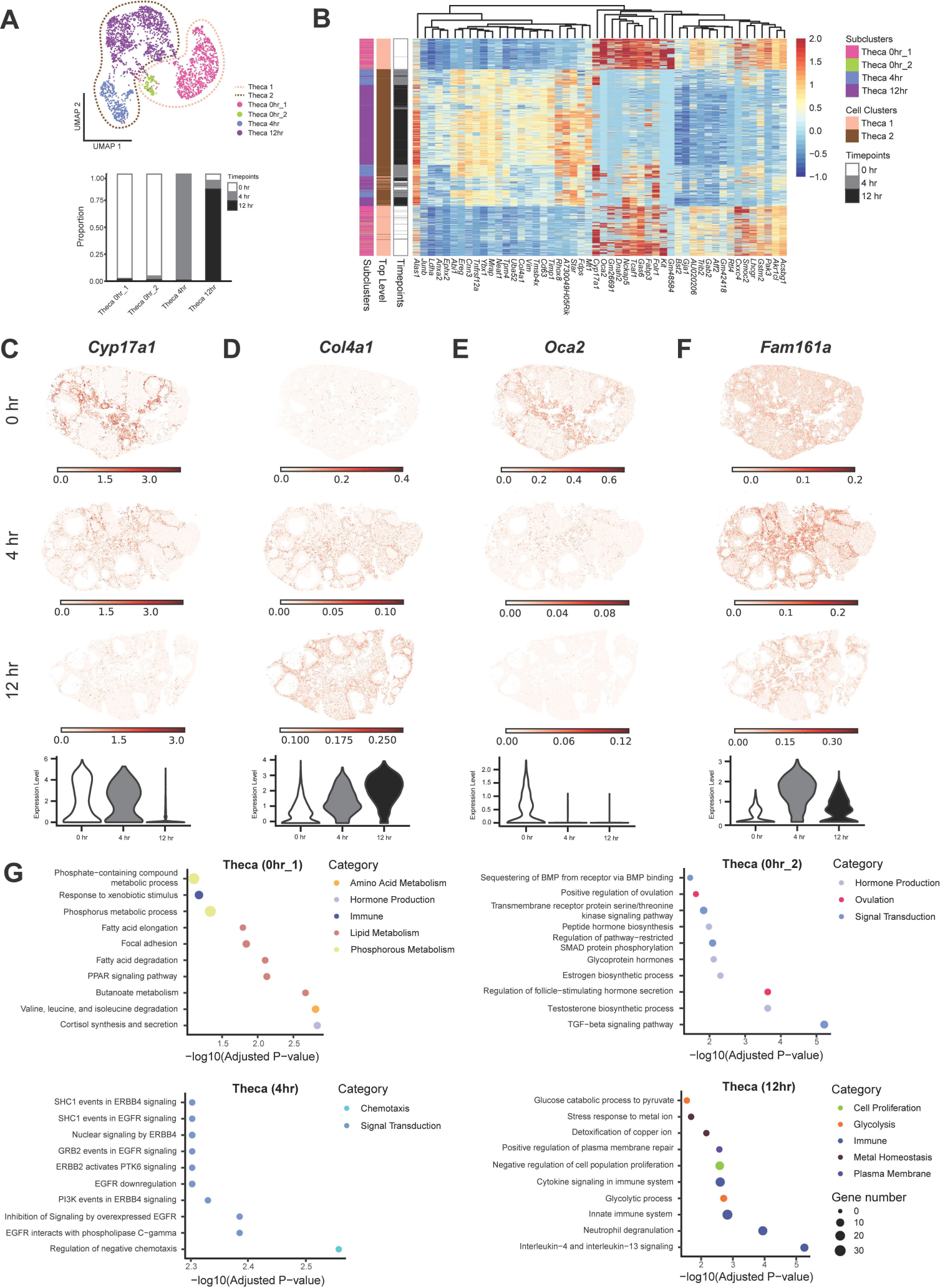
A
UMAP 2
UMAP 1
Theca 1
Theca 2
Theca 0hr_1
Theca 0hr_2
Theca 4hr
Theca 12hr
Proportion
Timepoints
0 hr
4 hr
12 hr
B
Subclusters
Top Level
Timepoints
Cell Clusters
C
Cyp17a1
D
Col4a1
E
Oca2
F
Fam161a
Expression Level
G
Theca (0hr_1)
Category
Amino Acid Metabolism
Hormone Production
Immune
Lipid Metabolism
Phosphorous Metabolism
Phosphate−containing compound metabolic process
Response to xenobiotic stimulus
Phosphorus metabolic process
Fatty acid elongation
Focal adhesion
Fatty acid degradation
PPAR signaling pathway
Butanoate metabolism
Valine, leucine, and isoleucine degradation
Cortisol synthesis and secretion
−log10(Adjusted P−value)
Theca (0hr_2)
Ovulation
Signal Transduction
Sequestering of BMP from receptor via BMP binding
Positive regulation of ovulation
Transmembrane receptor protein serine/threonine kinase signaling pathway
Peptide hormone biosynthesis
Regulation of pathway−restricted SMAD protein phosphorylation
Glycoprotein hormones
Estrogen biosynthetic process
Regulation of follicle−stimulating hormone secretion
Testosterone biosynthetic process
TGF−beta signaling pathway
Theca (4hr)
Chemotaxis
Signal Transduction
SHC1 events in ERBB4 signaling
SHC1 events in EGFR signaling
Nuclear signaling by ERBB4
GRB2 events in EGFR signaling
ERBB2 activates PTK6 signaling
EGFR downregulation
PI3K events in ERBB4 signaling
Inhibition of Signaling by overexpressed EGFR
EGFR interacts with phospholipase C−gamma
Regulation of negative chemotaxis
Theca (12hr)
Cell Proliferation
Glycolysis
Immune
Metal Homeostasis
Plasma Membrane
Glucose catabolic process to pyruvate
Stress response to metal ion
Detoxification of copper ion
Positive regulation of plasma membrane repair
Negative regulation of cell population proliferation
Cytokine signaling in immune system
Glycolytic process
Innate immune system
Neutrophil degranulation
Interleukin−4 and interleukin−13 signaling
Gene number

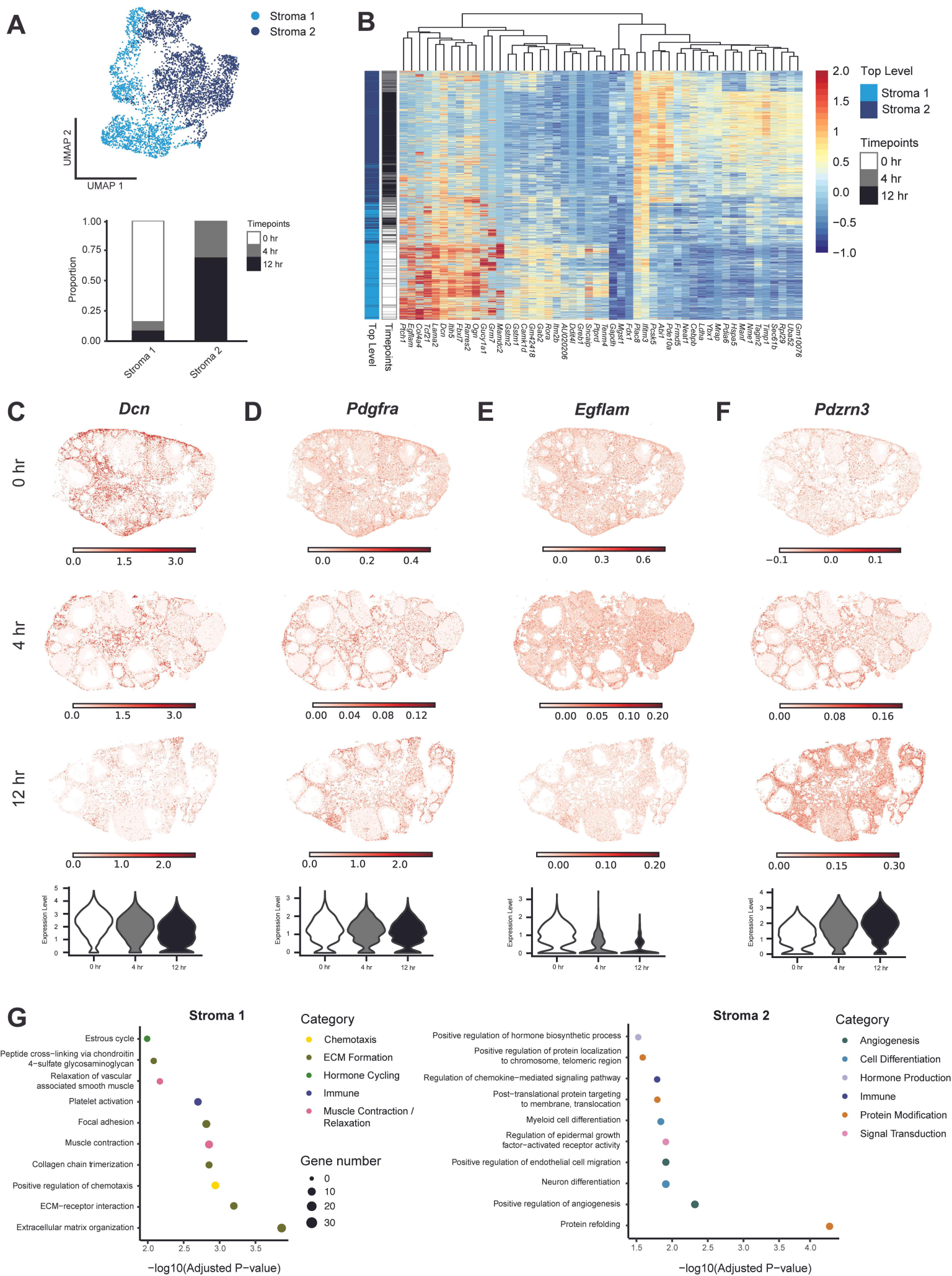
A
Stroma 1
Stroma 2
UMAP 2
UMAP 1
Proportion
Timepoints
0 hr
4 hr
12 hr
B
Top Level
Timepoints
Stroma 1
Stroma 2
C
Dcn
D
Pdgfra
E
Egflam
F
Pdzrn3
0 hr
4 hr
12 hr
Expression Level
G
Stroma 1
Estrous cycle
Peptide cross−linking via chondroitin 4−sulfate glycosaminoglycan
Relaxation of vascular associated smooth muscle
Platelet activation
Focal adhesion
Muscle contraction
Collagen chain trimerization
Positive regulation of chemotaxis
ECM−receptor interaction
Extracellular matrix organization
−log10(Adjusted P−value)
Category
Chemotaxis
ECM Formation
Hormone Cycling
Immune
Muscle Contraction / Relaxation
Gene number
Stroma 2
Positive regulation of hormone biosynthetic process
Positive regulation of protein localization to chromosome, telomeric region
Regulation of chemokine−mediated signaling pathway
Post−translational protein targeting to membrane, translocation
Myeloid cell differentiation
Regulation of epidermal growth factor−activated receptor activity
Positive regulation of endothelial cell migration
Neuron differentiation
Positive regulation of angiogenesis
Protein refolding
−log10(Adjusted P−value)
Category
Angiogenesis
Cell Differentiation
Hormone Production
Immune
Protein Modification
Signal Transduction

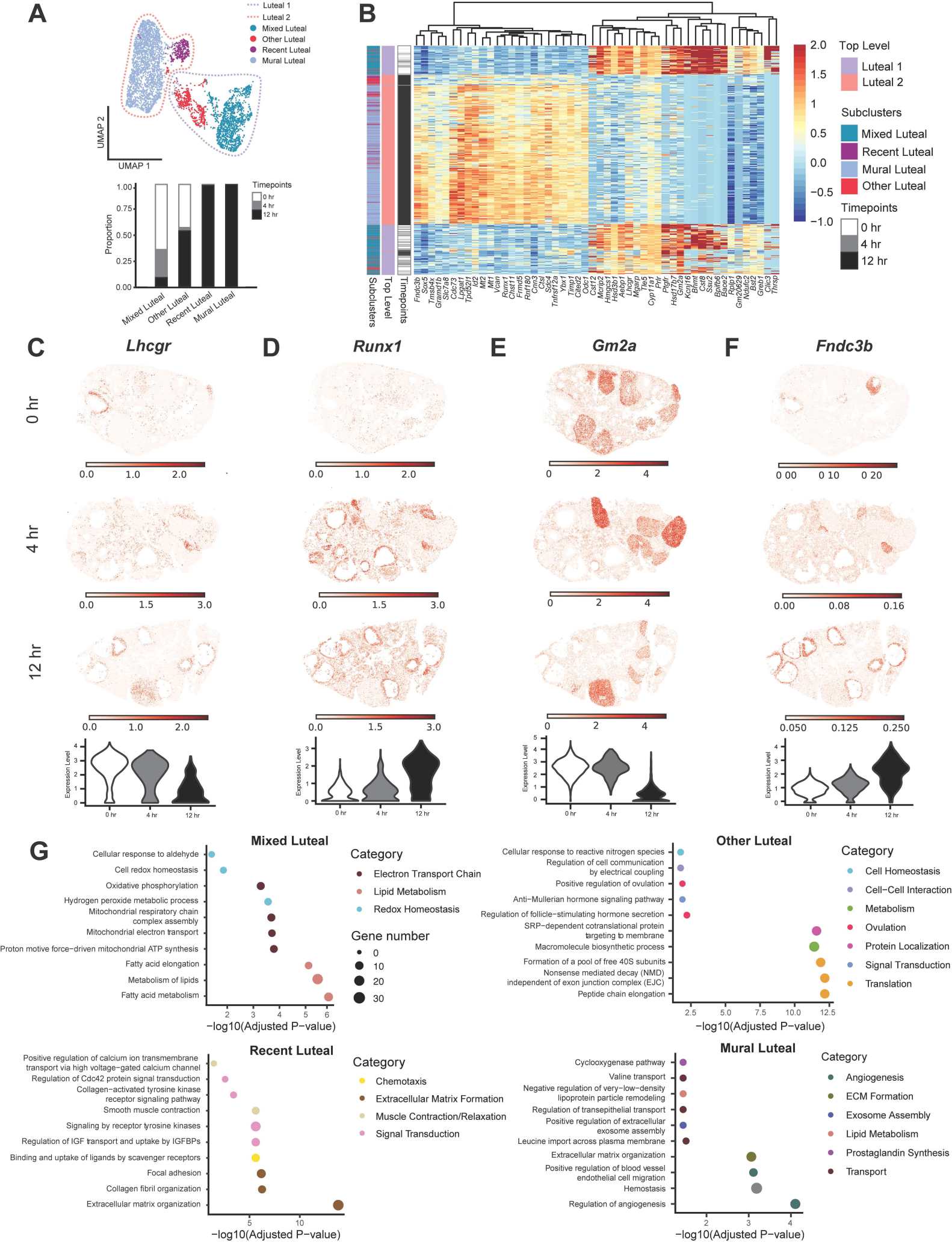
A
Luteal 1
Luteal 2
Mixed Luteal
Other Luteal
Recent Luteal
Mural Luteal
UMAP 2
UMAP 1
Timepoints
0 hr
4 hr
12 hr
Proportion
Mixed Luteal
Other Luteal
Recent Luteal
Mural Luteal
B
Top Level
Luteal 1
Luteal 2
Subclusters
Mixed Luteal
Recent Luteal
Mural Luteal
Other Luteal
Timepoints
0 hr
4 hr
12 hr
Subclusters
Top Level
Timepoints
C
Lhcgr
D
Runx1
E
Gm2a
F
Fndc3b
0 hr
4 hr
12 hr
Expression Level
G
Mixed Luteal
Cellular response to aldehyde
Cell redox homeostasis
Oxidative phosphorylation
Hydrogen peroxide metabolic process
Mitochondrial respiratory chain complex assembly
Mitochondrial electron transport
Proton motive force−driven mitochondrial ATP synthesis
Fatty acid elongation
Metabolism of lipids
Fatty acid metabolism
−log10(Adjusted P−value)
Category
Electron Transport Chain
Lipid Metabolism
Redox Homeostasis
Gene number
0
10
20
30
Other Luteal
Cellular response to reactive nitrogen species
Regulation of cell communication by electrical coupling
Positive regulation of ovulation
Anti−Mullerian hormone signaling pathway
Regulation of follicle−stimulating hormone secretion
SRP−dependent cotranslational protein targeting to membrane
Macromolecule biosynthetic process
Formation of a pool of free 40S subunits
Nonsense mediated decay (NMD) independent of exon junction complex (EJC)
Peptide chain elongation
−log10(Adjusted P−value)
Category
Cell Homeostasis
Cell−Cell Interaction
Metabolism
Ovulation
Protein Localization
Signal Transduction
Translation
Recent Luteal
Positive regulation of calcium ion transmembrane transport via high voltage−gated calcium channel
Regulation of Cdc42 protein signal transduction
Collagen−activated tyrosine kinase receptor signaling pathway
Smooth muscle contraction
Signaling by receptor tyrosine kinases
Regulation of IGF transport and uptake by IGFBPs
Binding and uptake of ligands by scavenger receptors
Focal adhesion
Collagen fibril organization
Extracellular matrix organization
−log10(Adjusted P−value)
Category
Chemotaxis
Extracellular Matrix Formation
Muscle Contraction/Relaxation
Signal Transduction
Mural Luteal
Cyclooxygenase pathway
Valine transport
Negative regulation of very−low−density lipoprotein particle remodeling
Regulation of transepithelial transport
Positive regulation of extracellular exosome assembly
Leucine import across plasma membrane
Extracellular matrix organization
Positive regulation of blood vessel endothelial cell migration
Hemostasis
Regulation of angiogenesis
−log10(Adjusted P−value)
Category
Angiogenesis
ECM Formation
Exosome Assembly
Lipid Metabolism
Prostaglandin Synthesis
Transport

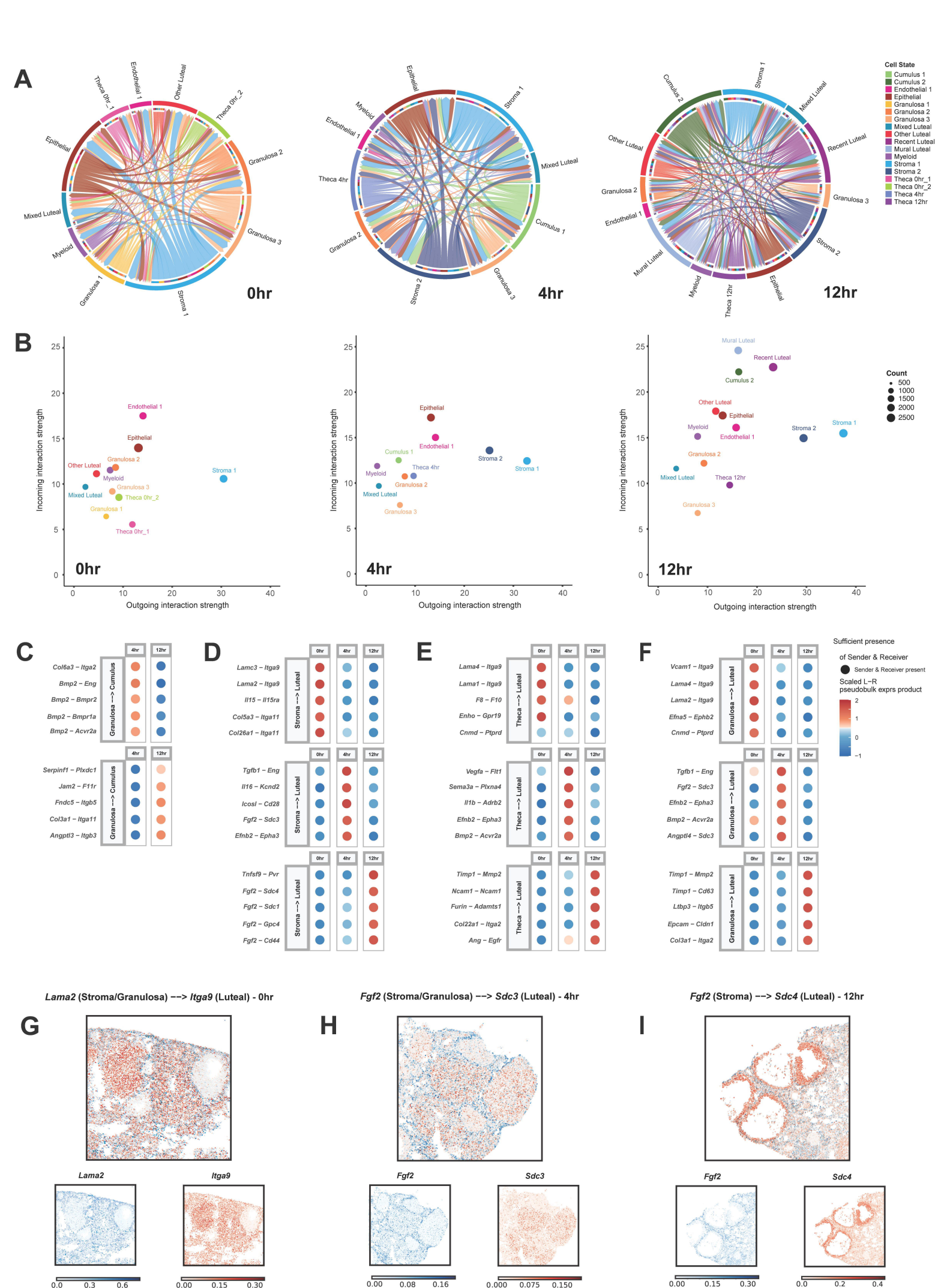
A
0hr
4hr
12hr
Cell State
Cumulus 1
Cumulus 2
Endothelial 1
Epithelial
Granulosa 1
Granulosa 2
Granulosa 3
Mixed Luteal
Other Luteal
Recent Luteal
Mural Luteal
Myeloid
Stroma 1
Stroma 2
Theca 0hr_1
Theca 0hr_2
Theca 4hr
Theca 12hr
B
Incoming interaction strength
Outgoing interaction strength
Count
500
1000
1500
2000
2500
C
Granulosa ---> Cumulus
Col6a3 – Itga2
Bmp2 – Eng
Bmp2 – Bmpr2
Bmp2 – Bmpr1a
Bmp2 – Acvr2a
Serpinf1 – Plxdc1
Jam2 – F11r
Fndc5 – Itgb5
Col3a1 – Itga11
Angptl3 – Itgb3
D
Stroma ---> Luteal
Lamc3 – Itga9
Lama2 – Itga9
Il15 – Il15ra
Col5a3 – Itga11
Col26a1 – Itga11
Tgfb1 – Eng
Il16 – Kcnd2
Icosl – Cd28
Fgf2 – Sdc3
Efnb2 – Epha3
Tnfsf9 – Pvr
Fgf2 – Sdc4
Fgf2 – Sdc1
Fgf2 – Gpc4
Fgf2 – Cd44
E
Theca ---> Luteal
Lama4 – Itga9
Lama1 – Itga9
F8 – F10
Enho – Gpr19
Cnmd – Ptprd
Vegfa – Flt1
Sema3a – Plxna4
Il1b – Adrb2
Efnb2 – Epha3
Bmp2 – Acvr2a
Timp1 – Mmp2
Ncam1 – Ncam1
Furin – Adamts1
Col22a1 – Itga2
Ang – Egfr
F
Granulosa ---> Luteal
Vcam1 – Itga9
Lama4 – Itga9
Lama2 – Itga9
Efna5 – Ephb2
Cnmd – Ptprd
Tgfb1 – Eng
Fgf2 – Sdc3
Efnb2 – Epha3
Bmp2 – Acvr2a
Angptl4 – Sdc3
Timp1 – Mmp2
Timp1 – Cd63
Ltbp3 – Itgb5
Epcam – Cldn1
Col3a1 – Itga2
Sufficient presence
of Sender & Receiver
Sender & Receiver present
Scaled L–R
pseudobulk exprs product
G
Lama2 (Stroma/Granulosa) --> Itga9 (Luteal) - 0hr
Lama2
Itga9
H
Fgf2 (Stroma/Granulosa) --> Sdc3 (Luteal) - 4hr
Fgf2
Sdc3
I
Fgf2 (Stroma) --> Sdc4 (Luteal) - 12hr
Fgf2
Sdc4